

A driven quantum superconducting circuit with multiple tunable degeneracies

Jayameenakshi Venkatraman,^{*} Rodrigo G. Cortiñas,^{*} Nicholas E. Frattini,[†] Xu Xiao, and Michel H. Devoret[‡]
Department of Applied Physics and Department of Physics, Yale University, New Haven, CT 06520, USA
 (Dated: May 11, 2023)

We present the experimental discovery of multiple simultaneous degeneracies in the spectrum of a Kerr oscillator subjected to a squeezing drive. This squeezing, in combination with the Kerr interaction creates an effective static two-well potential in the frame rotating at half the frequency of the sinusoidal driving force. Remarkably, these degeneracies can be turned on-and-off on demand, and their number is tunable. We find that when the detuning Δ between the frequency of the oscillator and characteristic frequency of the drive equals an even multiple of the Kerr coefficient K , $\Delta/K = 2m$, the oscillator displays $m + 1$ exact, parity-protected, spectral degeneracies, insensitive to the drive amplitude. The degeneracies stem from the unusual destructive interference of tunnel paths in the classically forbidden region of the double well static effective potential that models our experiment. Exploiting this interference, we measure a peaked enhancement of the incoherent well-switching lifetime creating a super-protected cat qubit in the ground state manifold of our oscillator. Our results demonstrate the relationship between degeneracies and noise protection in quantum systems.

Introduction – Degeneracies and their connection to symmetries play a pivotal role in physics. This connection leads to the emergence of noise-protected manifold of states for encoding and processing quantum information. For example, topological quantum systems exhibit global symmetries that result in degenerate ground states with inherent protection against local noise [1]. To error-correct a quantum computation, the information must be protected by a symmetry such that the environment is blind to any unitary taking place within the manifold of states [2, 3].

Atoms, like the hydrogen atom, exemplify the connection between symmetries and degeneracies through energy level degeneracies connected to spherical symmetry [4, 5]. Superconducting circuits implement artificial atomic and molecular physics Hamiltonians with the virtue of in-situ tunability of parameters [6]. The pursuit of noise protection has led to the proposal and investigation of complex novel circuits, such as the $0 - \pi$ qubit [7], whose near-degenerate qubit states are endowed with inherent resilience to decay and dephasing. However, the realization of such protected qubits often demands stringent circuit parameters.

In this work, we demonstrate an alternative approach to achieving circuit-level noise protection by employing a simple quantum nonlinear system, and engineering tunable spectral degeneracies within it. Our system consists of a sinusoidally-driven underdamped nonlinear oscillator. We realize a quantum double well with multiple degeneracies that can be turned on and off simply by

varying the frequency of the drive. Specifically, when the detuning Δ between the frequency of the oscillator and the characteristic frequency of the drive equals an even multiple of the Kerr coefficient K , $\Delta/K = 2m$, the oscillator displays $m + 1$ exact, parity-protected, spectral degeneracies that are insensitive to the drive amplitude. Remarkably, these degeneracies correspond to the complete suppression of tunneling for excited states below the barrier in a double-well potential of finite height [8].

Our experiment not only realizes for the first time, an elementary quantum optical system investigated theoretically [8–10] and uncovers new properties but also demonstrates new means to fight decoherence [11]. Specifically, we show that the quantum states at the bottom of the double well form a qubit manifold with a peaked interwell transition lifetime, a phenomenon we name *super-protection*, while remaining addressable. Thus, this qubit provides the basis for fault-tolerant syndrome measurement in quantum error correction [12, 13].

Model system – We introduce our experimental system as a sinusoidally driven superconducting quantum circuit oscillator described by the time-dependent Hamiltonian

$$\hat{\mathcal{H}}(t)/\hbar = \omega_o \hat{a}^\dagger \hat{a} + \frac{g_3}{3} (\hat{a} + \hat{a}^\dagger)^3 + \frac{g_4}{4} (\hat{a} + \hat{a}^\dagger)^4 - i\Omega_d (\hat{a} - \hat{a}^\dagger) \cos \omega_d t, \quad (1)$$

where ω_o is the small oscillation frequency and $g_3, g_4 \ll \omega_o$ are the third and fourth-rank nonlinearities of the oscillator, \hat{a} is the bosonic annihilation operator, and where the drive is specified by its amplitude Ω_d and frequency ω_d . Equation (1) models a SNAIL transmon that is charge-driven at frequency ω_d . It is the electrical circuit analog of an asymmetric mechanical pendulum capable of three and four-wave mixing [14]. The experimental setup has been described in [15]. The drive is configured so that its second subharmonic $\omega_d/2$ lies in the vicinity of the SNAIL transmon resonance at $\omega_a = \omega_o + 3g_4 - 20g_3^2/3\omega_o + \mathcal{O}(g_3^3/\omega_o^2)$.

^{*} jaya.venkat@yale.edu,rodrigo.cortinas@yale.edu; these two authors contributed equally.

[†] Present address: JILA, National Institute of Standards and Technology and the University of Colorado, Boulder, Colorado 80309, USA; Department of Physics, University of Colorado, Boulder, Colorado 80309, USA

[‡] michel.devoret@yale.edu

Under an approximation beyond the rotating-wave that captures the averaged behaviour of this rapidly driven nonlinear superconducting circuit, the dynamics governed by Eq. (1) is well-described by the static effective Hamiltonian [15–17]

$$\hat{H}/\hbar = \Delta \hat{a}^\dagger \hat{a} - K \hat{a}^{\dagger 2} \hat{a}^2 + \epsilon_2 (\hat{a}^{\dagger 2} + \hat{a}^2). \quad (2)$$

Equation (2) corresponds to an elementary quantum system: a Kerr oscillator dressed by a squeeze-drive. In Eq. (2), the detuning parameter is given by $\Delta = \Delta^{\text{bare}} + \delta^{\text{ac}}$, where $\Delta^{\text{bare}} = \omega_a - \omega_d/2$, with $|\Delta^{\text{bare}}| \ll \omega_a$, and where δ^{ac} corresponds to the ac Stark shift: $\delta^{\text{ac}} = (6g_4 - 9g_3^2/\omega_o + \mathcal{O}(g_3^3/\omega_o^2))|\Pi|^2$, where $|\Pi| = \Omega_d \omega_d / (\omega_d^2 - \omega_o^2)$. For our system, we measure $\omega_a/2\pi = 6.035$ GHz. The Kerr coefficient arises from the bare g_3 and g_4 nonlinearities of the circuit, which are themselves controlled in situ by a magnetic field, and is given by $K = 10g_3^2/3\omega_o - 3g_4/2 + \mathcal{O}(g_3^3/\omega_o^2)$. In our experiment, we measure it to be $K/2\pi = 316.8$ kHz (see Fig. 1). A crucial component of the experiment, the squeezing drive amplitude $\epsilon_2 = g_3|\Pi|$, is generated by the near-resonant three-wave mixing process between one drive excitation and two oscillator excitations. Due to the relatively small K compared to a standard transmon [6], our experiment has a negligible ac Stark shifts for $\epsilon_2/K \lesssim 1$, so that in this regime $\delta^{\text{ac}}/K \lesssim 1\%$. Therefore, in this regime, Δ can be approximated by $\Delta^{\text{bare}} = \omega_a - \omega_d/2$. By taking K to provide the natural units for our system, the Hamiltonian is completely determined by only two dimensionless parameters: Δ/K and ϵ_2/K , where the former is controlled by the drive frequency and the latter is directly proportional to the drive amplitude. We thus have independent real-time control of all relevant Hamiltonian parameters. Lastly, in our experiment, the single-photon lifetime of the undriven SNAIL transmon is $T_1 = 20$ μs and the Ramsey coherence between its lowest-lying eigenstates is $T_{2\text{R}} = 3.8$ μs .

Experiment and results – We first experimentally demonstrate the cancellation of tunneling in the ground state manifold. In Figure 1A, we show the classical limit of the energy surface associated with Eq. (2) for $\Delta/K = 3, \epsilon_2/K = 0.11$, as a function of phase-space coordinates. The arrows indicate the two WKB tunneling paths [18]. Furthermore, we show in Figure 1B, the wavefunctions corresponding to the ground state manifold. Note that these are not the energy eigenstates but their even and odd superpositions, which are localized in the left and right wells. Importantly, in the classically forbidden region, marked in grey, oscillations accompany the expected decay of the wavefunctions [8]. To observe coherent cancellation of tunneling in the ground state manifold, we prepare a localized well state and measure its tunneling probability as a function of time for different values of Δ and ϵ_2 . We present the measurement protocol in Figure 1C. The preparation is done by rapidly turning on the squeezing drive until an amplitude of $\epsilon_2/K = 8.7$ is reached. We subsequently wait for $5T_1$

for the system to relax to its steady state in the presence of the squeezing drive and measure, in a quantum non-demolition (QND) manner, the quadrature containing the which-well information. This measurement projects the system into one of the wells. It is done by the microwave activation of a parametric beam splitter interaction between the squeeze-driven Kerr oscillator and a readout resonator strongly coupled to a quantum-limited amplifier chain. We refer the reader to [15] for experimental details, where the preparation-by-measurement procedure for our system was introduced. This readout protocol yields a stabilized fluorescence signal revealing the quadrature measurement outcome, while the squeezing drive sustains the circuit oscillation. After the preparation, we adiabatically lower the squeezing drive amplitude in a duration $1.6 \mu\text{s} \gtrsim \pi/K$.¹ The depth of the wells, which increases with ϵ_2/K (see supplement), is then reduced so that the tunnel effect becomes observable. We then wait for a variable amount of time before adiabatically raising the squeezing drive amplitude to its initial value. Finally, we measure which well the system has adopted.

The data for this tunneling measurement is shown in Figure 1D, where we interpret the oscillating color pattern as tunnel-driven Rabi oscillations. The periodic cancellation of tunneling at $\Delta/K = 2m$, where m is a non-negative integer, is clearly visible as a divergence of the Rabi period. We extract the tunneling amplitude $|\delta E|$ from our data by fitting the oscillation frequency with an exponentially decaying sinusoid and plot this frequency in Figure 1E, where the data-point color corresponds to the value of ϵ_2 (see supplement for calibration of ϵ_2). The black lines, obtained from an exact diagonalization of the static effective Hamiltonian Eq. (2), correspond to the energy difference between levels in the ground state manifold. The cancellation of tunneling for the ground state manifold in a parametrically modulated oscillator was predicted by [8] where, using a semiclassical WKB method, the authors found that this multi-path interference effect is due to, and accompanied by, oscillations of the wavefunction crossing zero in the classically forbidden region. Here, we find good agreement between our experiment and their WKB prediction (see supplement). Note that, across the zero of the tunneling amplitude, the bonding and anti-bonding superposition of well states alternate as the ground state. Specifically, for $\Delta/K = 4m + 1$, the ground state is the bonding superposition of well states (see supplement). In Fig. 1F, we further plot the extracted decay time of the tunneling oscillations as a function of Δ , and find sharp peaks when $\Delta/K = 2m$, besides an overall continuous increase of the

¹ Note that this adiabaticity condition pertains to the gap between the ground and first excited pair of states. We do not need to be adiabatic with respect to the two tunnel split states within the ground state manifold since they have opposite parity and the parity preserving squeezing drive will not couple them.

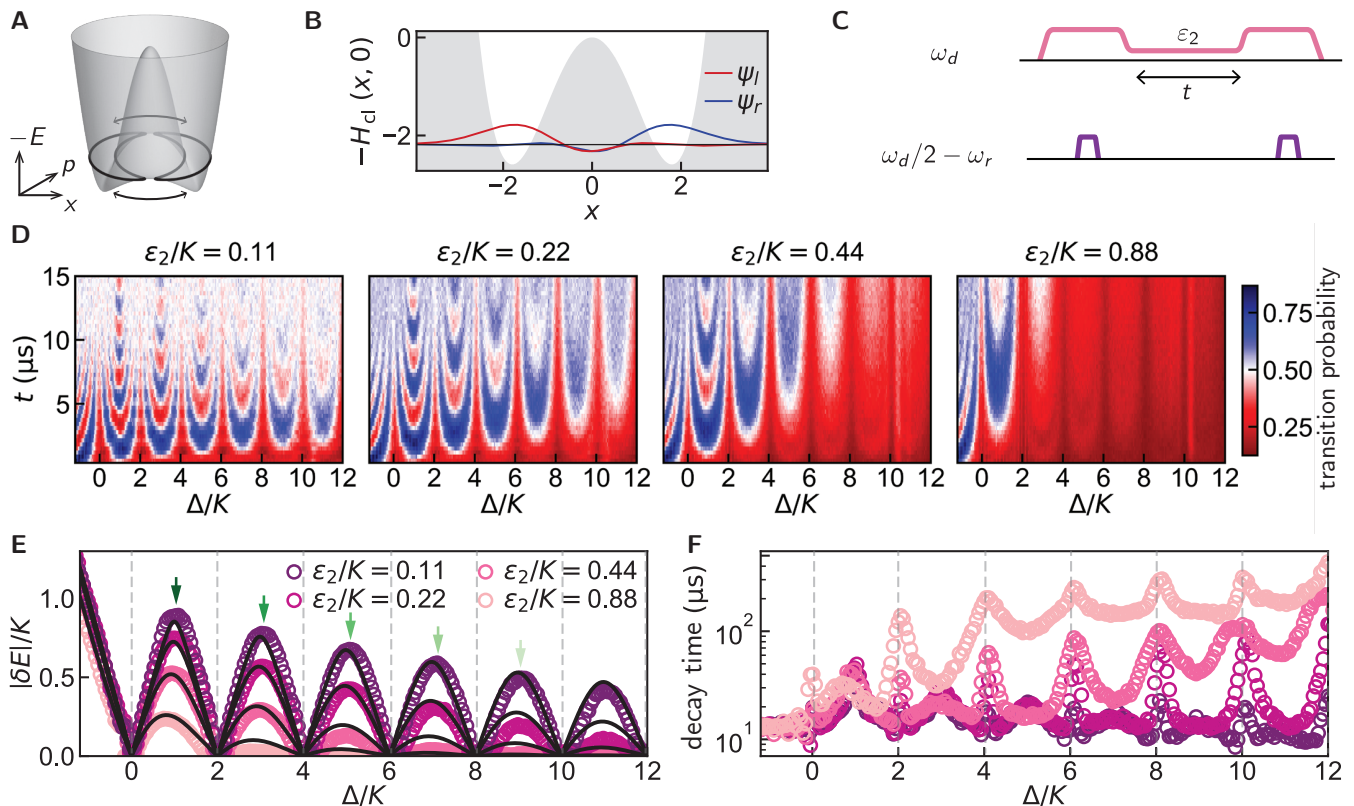


FIG. 1. **Tunnel-driven Rabi oscillations in the ground state manifold and their periodic cancellation.** **A** Energy surface associated with Eq. (2) in the classical limit for $\Delta/K = 3$ and $\epsilon_2/K = 0.11$. The orbits shown with black lines are obtained by semiclassical action quantization and represent the ground states (see supplement). Bidirectional arrows represent the two interfering WKB tunneling paths. **B** Cut of the energy surface in **A** at $p = 0$ (see supplement). The classically forbidden region is marked in grey. The left and right localized wavefunctions are indicated in red and blue. **C** Pulse sequence for **D**. The pink line represents the squeezing drive at frequency ω_d and the purple lines represent the preparation and readout drives at frequency $\omega_d/2 - \omega_r$. **D** Time-domain Rabi oscillation measurement of inter-well tunneling probability (color) as a function of Δ^{bare} , taken here as Δ (see text), for $\epsilon_2/K = 0.11, 0.22, 0.44$, and 0.88 . The extracted tunneling amplitudes from **D** are shown as open circles in **E**. The black lines in **E** correspond to the transition energy between the lowest eigenstates obtained from an exact diagonalization of Eq. (2). A comparison of the extracted tunneling rate with a semiclassical WKB calculation is presented in the supplement. Green arrows in **E** denote the condition for constructive interference of tunneling and correspond to the measurements shown in Figure 2. We extract the value of the Kerr coefficient K from this data and note that it is consistent, within experimental inaccuracies, with an independent saturation spectroscopy measurement of the Fock qubit in the absence of the squeezing drive (see supplement). **F** Decay time of the tunnel-driven Rabi oscillations for different values of Δ and ϵ_2 in **D**. Sharp peaks in the decay time are clearly visible for $\Delta/K = 2m$, m being a non-negative integer.

decay time with Δ and ϵ_2 . The peaks at $\Delta/K = 2m$ arise from the degeneracies in the excited state spectrum at this condition and are discussed later in the text.

Importantly, the dynamics of the two-level system in Figure 1D suggest a new type of bosonic encoding of information that we call the Δ -Kerr-cat qubit. The north and south poles of the corresponding Bloch sphere, a generalization of the $\Delta = 0$ one [15, 17, 19], is defined by the cat states formed by the lowest pair of eigenstates of Eq. (2). In this picture, a tunnel-Rabi cycle in Figure 1D for a fixed $\Delta/K \neq 2m$ corresponds to a travel along the equator. For $\Delta/K = 2m$, this travel is prohibited. Note that when $\Delta/K = 2m + 1$, the tunneling amplitude is maximum and is first-order insensitive to fluctuations of Δ .

From Figure 1E, we also see that, besides the *discrete cancellation* of tunneling at $\Delta/K = 2m$, tunneling in the ground state manifold is overall *continuously reduced* with both Δ and ϵ_2 . This reflects the well-known symmetry of the double well, which is broken by tunnel coupling. The approximate symmetry is restored with increasing Δ and ϵ_2 because both parameters explicitly control the barrier height and thus exponentially control the tunneling amplitude $|\delta E|$. Theory predicts that the larger the detuning Δ , the faster the tunneling reduction with the squeezing drive amplitude ϵ_2 (see supplement). We have measured this effect by measuring the tunneling amplitude as a function of ϵ_2 for different constructive tunneling conditions corresponding to $\Delta/K = 2m + 1$. The data is presented in Figure 2. The exponential insensi-

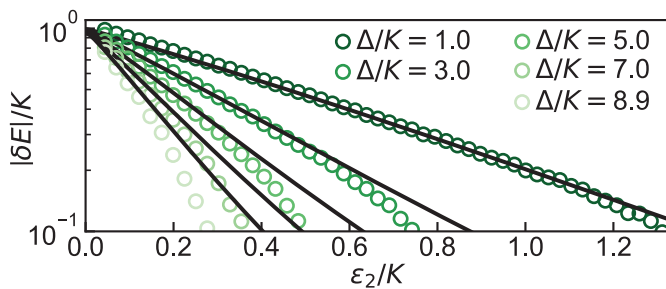


FIG. 2. **Exponential reduction of tunnel splitting as a function of ϵ_2 in the ground state manifold.** Extracted tunnel splitting (open circles) for the first five local maxima in Figure 1E as marked by the color coded arrows. Experimental sequence as in Figure 1E. For the raw color data, see Figure 3 in the supplement. Black lines are obtained from a Hamiltonian diagonalization of Eq. (2) with no adjustable parameters. For comparison with a semiclassical WKB calculation, see supplement. Note that for small tunneling amplitude, dissipation plays a relevant role and the Hamiltonian model used here is insufficient.

tivity, around $\Delta = 0$, to fluctuations of Δ due to a noisy ω_a , as a function of ϵ_2 , was predicted by [19] and thus proposed as a resource for quantum information. This insensitivity was a key motivation for realizing the Kerr-cat qubit experimentally [17]. The insensitivity of the ground state manifold to detuning as a function of ϵ_2 is directly observed here for the first time. Note from Figure 1E that for $\Delta < 0$, in the parameter regime $\epsilon_2/K < 1$, the tunneling amplitude $|\delta E|$ is weakly dependent on ϵ_2 , whereas for $\Delta > 0$, it is strongly dependent on ϵ_2 . This weak dependence for $\Delta < 0$ is expected since the barrier height vanishes for small values of ϵ_2/K .² Our finding shows that new operating points at even, positive values of Δ/K will increase the resilience of ground-state qubit encoding to detuning-like noise.

Moving to the pairs of excited states above the ground state manifold, do they also present observable degeneracies as a function of Δ/K ? In order to deepen our understanding of this problem, we first examine the classical energy surface associated with Eq. (2) via the period doubling phase diagram [20] shown in Figure 3A. In the classical limit (see supplement), the parameter space spanned by Δ/K and ϵ_2/K is divided by two phase transitions located at $\Delta = \pm 2\epsilon_2$. The different phases are characterized by the number of stable nodes (attractors) in the classical metapotential and we refer to them as the single-, double-, and triple-node phases. These phases correspond to different metapotential topologies. We show them as contour line

insets in Figure 3A, representing classical orbits. The single-node phase occurs for $\Delta < -2\epsilon_2$, and presents only one well. For $\Delta \geq -2\epsilon_2$, the oscillator has bifurcated and the classical metapotential acquires two wells. In the presence of dissipation, these wells house stable nodes. The emergent ground state manifold has been exploited, for $\Delta = 0$, in the Kerr-cat qubit [15, 17]. In the interval $-2\epsilon_2 \leq \Delta < 2\epsilon_2$, an unstable extremum (saddle point) appears at the origin. For $\Delta \geq 2\epsilon_2$, the saddle point at the origin splits into two saddle points and an attractor reappears at the origin. The barrier height of the classical metapotential is given by $(\Delta + 2\epsilon_2)^2/4K$ in the double-node phase and by $2\epsilon_2\Delta/K$ in the triple-node phase (see supplement). To count the number of excited states that have sunk under the barrier, we further introduce in Figure 3B a semi-classical phase diagram of the squeeze-driven Kerr oscillator. Following the Einstein-Brillouin-Keller method, which generalizes the notion of Bohr orbits, we quantize the action enclosed in the metapotential well below the height of the barrier and obtain the number of in-well excited states. In Figure 3C, we present the corresponding orbits in the energy surface for a fixed value of $\epsilon_2/K = 2.17$ and four values of Δ/K . We validate this simple, semiclassical picture with a fully quantum mechanical calculation of the Wigner functions of localized states in the ground and excited state manifold (see supplement). It is clear from this analysis that, by increasing ϵ_2 and Δ , and therefore the barrier height, not only the ground state manifold but even the excited state manifolds become progressively ensconced in the wells, and we thus expect the tunneling between the wells to be drastically reduced.

Besides the overall *continuous reduction* of tunneling, the excited state manifold of the squeeze-driven Kerr oscillator experiences a *discrete cancellation* of tunneling when $\Delta/K = 2m$. Since the squeezing interaction preserves photon parity, levels belonging to the even and odd sector of the Kerr Hamiltonian remain decoupled and repeatedly cross at values of Δ/K corresponding to even integers. This braiding induces $m + 1$ perfect degeneracies at $\Delta/K = 2m$. Moreover, the corresponding eigenstates have a closed-form expression in the Fock basis. Remarkably, these features are independent of the value of ϵ_2 , reflecting a particular, unappreciated symmetry of our Hamiltonian Eq. (2) (see supplement).

Both the *discrete cancellation* and the overall *continuous reduction* of tunneling now in the excited state manifold of the squeeze-driven Kerr oscillator is accessed by performing spectroscopy measurements as a function of Δ , which we show in Figure 3F for $\epsilon_2/K = 2.17$. The measurement protocol is shown in Figure 3D. We prepare a localized well state in a manner that is similar to the protocols of Figures 1 and 2. To locate the frequency of the excited states, we apply a probe tone at variable frequency in the vicinity of the SNAIL transmon resonance ω_a and measure the well-switching probability. When the probe is resonant with a transition to a state close to the barrier maximum, this probability

² In the absence of dissipation, the metapotential acquires two wells as soon as $\epsilon_2, \Delta > 0$, i.e. there is no threshold for bifurcation of the driven oscillator. In our quantum experiment, this threshold is finite but is, relatively speaking, extremely small since and is set by $\epsilon_2^2 > (\Delta^2 + T_1^{-2}/4)/4$ (see [14]).

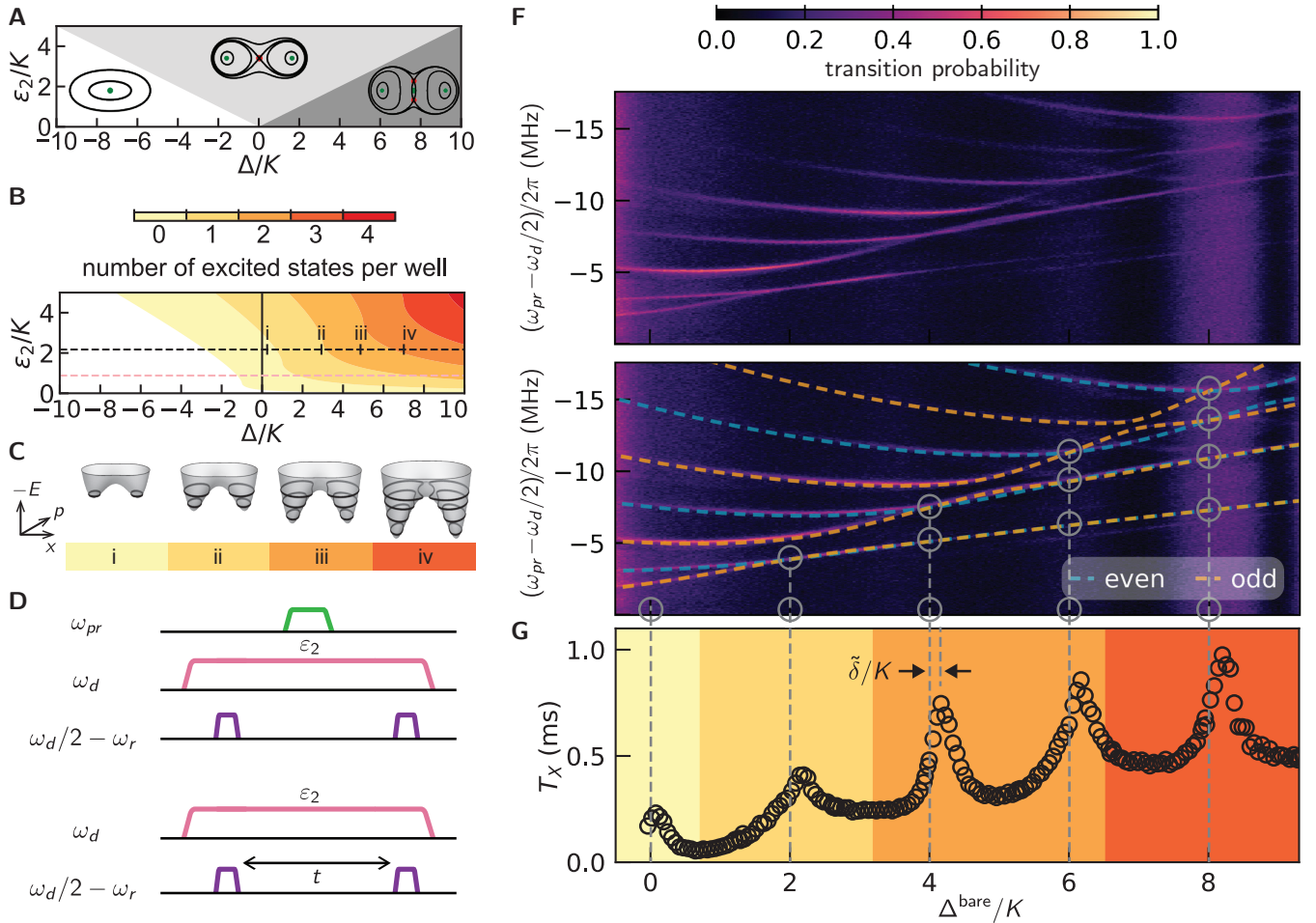


FIG. 3. Spectroscopic measurements of coherent and periodic cancellation of tunnel splitting in the excited state spectrum. **A** Classical phase diagram for the Kerr oscillator with parametric squeezing, also called the period-doubling bifurcation diagram. **B** Quantum phase diagram to count in-well excited states. White lines separate single-node, double-node, and triple-node phases. Colors represent contours of constant action on the energy surface associated with Eq. (2). Dashed pink line corresponds to $\epsilon_2/K = 0.88$, the maximum value of squeezing drive amplitude in Fig. 1. Dashed black line corresponds to $\epsilon_2/K = 2.17$, the value of squeezing drive amplitude used in Figs. 3F and 3G. Energy surfaces for $\epsilon_2/K = 2.17$ and (i) $\Delta/K = 0.5$, (ii) $\Delta/K = 3$, (iii) $\Delta/K = 5$, and (iv) $\Delta/K = 7$. Bohr-like orbits are indicated as black curves (see supplement for more details). **D** Pulse sequence for **F**. The green line represents the weak spectroscopic probe tone at frequency ω_{pr} . The pink line represents the squeezing drive at frequency ω_d and the purple lines represent the preparation and readout drives at frequency $\omega_d/2 - \omega_r$. **E** Pulse sequence for **G**. **F** (upper panel) Frequency-domain measurement of well-transition probability (color) via excited states as a function of Δ for $\epsilon_2/K = 2.17$. The power of the perturbative spectroscopic probe is increased as ω_{pr} is decreased to compensate for the lower matrix element connecting the ground state with the higher excited levels, yet is kept weak enough to preserve the parity conservation rules of Eq. (2). **F** (lower panel) Dashed lines plotted on top of experimental data (same as in upper panel) correspond to transition energies obtained by performing an exact diagonalization of Eq. (2) with no adjustable parameters. The Kerr coefficient is calibrated via time-domain measurements in Figure 1E. **G** Measured well-switching time under incoherent environmental-induced evolution as a function Δ for $\epsilon_2/K \approx 2.17$. Background color in **G** marks the number of excited states per well following semiclassical orbit quantization.

is increased. The experimental results are shown in Figure 3F. The colored dashed lines (orange and blue) in the lower panel are obtained from an exact diagonalization of the static effective Hamiltonian Eq. (2) with no adjustable parameters. The crossings of levels are accompanied by a continuous reduction of the braiding amplitude with Δ . The corresponding reduction of

the tunnel splitting is the manifestation associated with a generic double-well Hamiltonian while the braiding reflects interference specific to our particular Hamiltonian, resulting from its underlying driven character. The level of experimental control achieved allows us to observe in this data the joint presence of the *exact discrete symmetry* and the *approximate continuous symmetry* in our bosonic system.

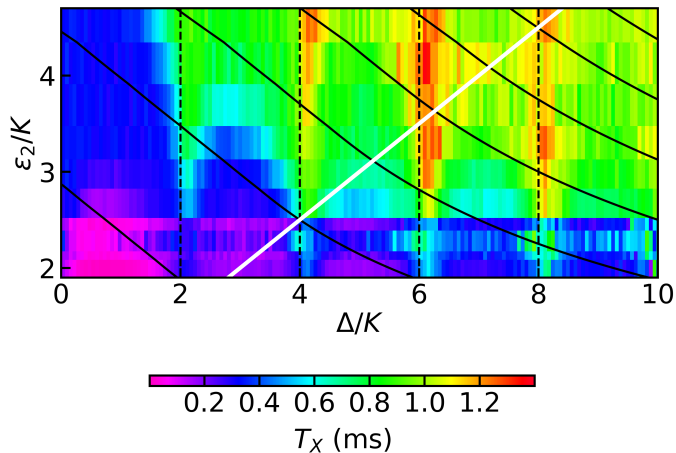


FIG. 4. **Color plot of T_X as a function of Δ/K and ϵ_2/K .** White line marks the transition from a two-node to a three-node metapotential. Black solid lines mark contours of constant barrier height. Increasing both Δ/K and ϵ_2/K yields fastest enhancement in T_X as predicted by Figure 3B. The additional enhancement by the coherent cancellation of excited state tunneling at $\Delta/K = 2m$ stands out. The pulse sequence for the measurement is shown in Figure 3E.

An important consequence of the cancellation of tunneling in the excited state spectrum is the periodic enhancement of the well-switching time under incoherent environment-induced evolution. This time scale corresponds to the transverse relaxation time, T_X , of a new bosonic qubit: a Δ -variant of the Kerr-cat qubit [14, 19] as mentioned earlier. To measure T_X , we prepare a localized well state by measurement, and wait for a variable amount of time before measuring the which-well information. We show the pulse sequence in Figure 3E. We obtain T_X by fitting a decaying exponential function to the measured well-transition probability for each value of Δ and plot the result in Figure 3G. Note that we have chosen the squeezing drive amplitude, identical to that of Figure 3F, as $\epsilon_2/K = 2.17$. Around values of Δ/K corresponding to even integers, the variation of T_X presents sharp peaks. The location of the peaks corresponds to the degeneracy condition in the excited state spectrum, associated with coherent cancellation of tunneling and the blocking of noise-induced well-switching pathways via the excited states. The systematic right-offset δ/K of each peak from an even integer, is 15%. About 5% can be attributed to the ac Stark shift δ^{ac} for this photon number, given the accuracy of our knowledge of the experimental parameters. We do not have an explanation for the remaining 10%, but we suspect it could be explained by higher-order terms in our static effective Hamiltonian. Note that this explanation is still compatible with the perfect alignment of the cancellation points with even integers in Figure 1F for $\epsilon_2/K < 1$, since for that case the ac Stark shift is negligible. Note also that this offset could provide access, within experimental ac-

curacy, via the ac Stark shift, to the nonlinear parameters of Eq. (1).

The data in Figure 3G also shows that the discrete peaks are accompanied by a monotonic baseline increase, a direct manifestation of the overall continuous tunneling reduction in the spectrum versus Δ . The background colored stripes represent the number of in-well excited states found via the action quantization method discussed above and in the supplement. Continuing with this semiclassical picture, we interpret the slowdown in the growth of T_X for $\Delta/K \gtrsim 5$ as the slowdown in the growth of the barrier height as one crosses over from the double-node, where the barrier height $\propto (\Delta + 2\epsilon_2)^2$, to the triple-node phase, where the barrier height $\propto \Delta\epsilon_2$. Indeed, this is the quantum manifestation of the classical phase transition from the double-node to the triple-node phase.

Thus, whether the theoretical framework is classical, semiclassical, or quantum, the predicted T_X will increase with both ϵ_2 and Δ . While ϵ_2 and Δ contribute via the overall continuous reduction of tunneling [15], only Δ controls the discrete cancellation of tunneling. We verify this prediction by measuring T_X while varying simultaneously both Hamiltonian parameters. We present the result of this experiment in Figure 4. We further plot contours of constant barrier height in black, and the expected separation between the double-node and triple-node metapotential as a white line. The system lying deeply in the quantum regime, we do not expect any sharp features along this line. As expected, following the gradient of the barrier height, one observes the fastest gain in T_X , with a maximum of $T_X = 1.3$ ms for $\Delta/K = 6$ and $\epsilon_2/K = 4$. Increasing the lifetime by increasing ϵ_2 presents limitations, since strong drives are known to cause undesired effects in driven nonlinear systems (see [21, 22] and supplement).

One could argue that $\Delta = 0$ provides an important factorization condition that guarantees that the ground state manifold is spanned by exact coherent states (see [19] and supplement). Indeed, this is an asset for quantum information, since these states are eigenstates of the single-photon loss operator \hat{a} [23]. However, this desirable property is traded for the advantages discussed earlier when $\Delta/K = 2m$, $m \geq 1$. Even if the Δ -variant of the Kerr-cat qubit suffers from quantum heating and quantum diffusion [18, 24, 25] at zero temperature resulting from the squeezed nature of its ground states, these effects are small and, as we show in the experiments reported here and in [15], the well-states of the Kerr-cat live longer than its $\Delta = 0$ parent, even at finite temperature.

Discussion – Although quantum tunneling was discovered nearly a century ago [26] and observed since in a variety of natural and synthetic systems, the treatment of tunneling is usually limited to the ground states of the system and has rarely been discussed for excited states in the literature, as we elaborate in the following survey. The phenomenology of ground state tunneling has been studied in cold atoms [27] in three-dimensional optical

lattices [28], optical tweezers [29], ion traps [30] and in quantum dots [31]. In Josephson tunnel circuits, quantum tunneling of the phase variable was first observed by Devoret, Martinis, and Clarke [32] and since then exploited in several other experiments [33]. Furthermore, the tunnel effect has been involved in quantum simulation [34], in Floquet engineering of topological phases of matter and to generate artificial gauge fields with no static analog [35, 36]. The quantum interference of tunneling for the ground states of a large spin system was measured previously in a cluster of eight iron atoms by Wernsdorfer and Sessoli [37] (see also [38]).

Weilinga and Milburn [9] first identified that the quantum optical model in Eq. (2) exhibits ground state tunneling for a particular value of Δ . Marthaler and Dykman [8, 18] developed a WKB treatment for a range of the Δ parameter, and predicted that, for this model, the tunnel splitting of the ground state manifold crosses zero periodically and is accompanied by oscillation of the wavefunction in the classically forbidden region.

Our work is the first experimental realization of the longstanding theoretical proposals of the last paragraph. It is similar, but different, to the phenomenology of the “coherent destruction of tunneling”, discovered theoretically by Grossmann et al. [39] and observed experimentally in cold atoms [40, 41]. Indeed, the dynamical tunneling in our experiment is in sharp contrast with photon-assisted or suppressed tunneling in weakly driven double-well potentials. Firstly, our tunneling is completely dynamical, i.e., the tunneling barrier vanishes in the absence of the drive. Secondly, and most importantly, our work extends the coherent cancellation of tunneling to all the excited states in the well. The periodic resonance condition $\Delta/K = 2m$, shared for the $m + 1$ first pairs of excited levels, is independent of the drive amplitude. Remarkably, under this multi-state resonance condition, the first $2(m + 1)$ oscillator states have a closed-form expression in the Fock basis (see supplement). We further emphasize that the dynamical tunneling in our work is distinct from chaos-assisted dynamical tunneling [42] observations made in ultracold atoms over three decades ago [42, 43]; remarkably our strongly driven nonlinear system remains integrable. To the best of our knowledge, our work corresponds to the discovery and the first demonstration of the exact simultaneous cancellation of the tunnel splitting for the ground and excited states. Our data featuring the incoherent dynamics can be qualitatively modeled by a Lindbladian treatment that we present in the supplement, yet more research on the decoherence of driven nonlinear driven systems is needed to get a quantitative agreement (see [22]).

As a resource for quantum information, the squeeze-driven Kerr oscillator for $\Delta = 0$, was identified in theory proposals by Cochrane, Milburn, and Munro [44] and Puri, Boutin, and Blais [19] due to its exponential resilience to low frequency noise and was proposed for a bosonic code. The code was implemented for the first time in circuits [17]. Bistability for non-zero Δ was pre-

dicted by Roberts and Clerk in [45]. Our work demonstrates this bistability experimentally through the lifetime peaks in Fig. 3G and explains the peaks as a fingerprint of the observed spectral degeneracies in Fig. 3F. Furthermore, the resilience to noise in the non-zero Δ case is demonstrated through Fig. 1E and Fig. 2.

Conclusion – We have observed multiple degeneracies between pairs of states in a quantum double-well system, resulting from the interplay of quantum tunneling and quantum interference. Our work showcases the tunability of these degeneracies in number and the ability to rapidly activate or deactivate them. Furthermore, we have identified the drive frequency as a critical control parameter, governing not only a discrete exact symmetry in Eq. (2), manifested as exact degeneracies, but also a continuous approximate symmetry that leads to an overall exponential reduction of tunnel splitting in both ground and excited states of our oscillator. This high degree of quantum control culminates in a significant reduction of incoherent well-flip dynamics, enabling the creation of a super-protected cat-qubit—the Δ -Kerr-cat qubit. Our demonstration of the continuous Z-gate [12, 46] adds valuable capability to the single qubit gate-set for cat qubits, offering new tools for quantum computation [15, 17, 19, 23, 46–49]. With comprehensive control over the parameter space of an individual squeeze-driven Kerr oscillator and the ability to measure its spectrum as a function of these parameters, our system holds immense significance in the theories of Quantum Phase Transitions (QPT) [50], Excited State QPT (ESQPT) [51], and Dissipative QPT (DQPT) [52]. Incidentally, the phase portrait presented in Fig. 3A is very similar to the one in Figure 1 in [53]. Moreover, our findings underscore the potential of superconducting circuits for simulating symmetries, providing the unprecedented advantage of in situ tunability. This breakthrough opens up new research avenues in the simulation of atomic, molecular, and nuclear physics.

A quasi-spin symmetry and an algebraic structure underlying the measured degeneracies were recently discovered by F. Iachello and will be discussed in a forthcoming paper.

After our experiments were performed, we learned that the degeneracies in our squeeze-driven Kerr oscillator were studied theoretically by our colleagues in the QUANTIC group in INRIA, Paris [11].

Acknowledgements – We acknowledge Vladislav Kurilovich for pointing to us the peculiarity of the amplitude independence of the multi-level degeneracies in our model. We thank Charlotte G. L. Böttcher, Steven M. Girvin, Leonid Glazman, Francesco Iachello, Alessandro Miano, Shruti Puri, and Qile Su for useful discussions. R. G. C acknowledges useful discussions with Lea Santos, Mazyar Mirrahimi, Diego Ruiz, and Jérémie Guillaud. This research was sponsored by the Air Force Office of Scientific Research under award number FA9550-19-1-0399, by the Army Research Office (ARO) under grant numbers W911NF-18-1-0212 and W911NF-16-1-

0349, and by the National Science Foundation (NSF) under award numbers 1941583 and 2124511, and by the U.S. Department of Energy, Office of Science, National Quantum Information Science Research Centers, Co-design Center for Quantum Advantage (C2QA) under contract number DE-SC0012704. The views and conclusions contained in this document are those of the authors and should not be interpreted as representing the official policies, either expressed or implied, of the U.S. Government. The U.S. Government is authorized to reproduce and distribute reprints for Government purposes notwithstanding any copyright notation herein. Fabrication facilities use was supported by the Yale Institute for Nanoscience

and Quantum Engineering (YINQE) and the Yale SEAS Cleanroom.

Author contributions – N.E.F. designed the sample package and fabricated the device. N.E.F. and R.G.C. built the measurement setup. X.X. and J.V. identified Δ as a useful knob and J.V. proposed its experimental implementation. J.V. and R.G.C. designed and performed experiments and analyzed data. J.V. and R.G.C. performed theoretical calculations and simulations. M.H.D., X.X., and N.E.F. discussed the project with J.V. and R.G.C. and provided insight. J.V., R.G.C., and M.H.D. wrote the manuscript with input from all the authors.

-
- [1] M. Freedman, A. Kitaev, M. Larsen, and Z. Wang, Topological quantum computation, *Bulletin of the American Mathematical Society* **40**, 31 (2003).
- [2] N. Ofek, A. Petrenko, R. Heeres, P. Reinhold, Z. Leghtas, B. Vlastakis, Y. Liu, L. Frunzio, S. Girvin, L. Jiang, *et al.*, Extending the lifetime of a quantum bit with error correction in superconducting circuits, *Nature* **536**, 441 (2016).
- [3] R. Acharya, I. Aleiner, R. Allen, T. I. Andersen, M. Ansmann, F. Arute, K. Arya, A. Asfaw, J. Atalaya, R. Babush, D. Bacon, J. C. Bardin, J. Basso, A. Bengtsson, S. Boixo, G. Bortoli, A. Bourassa, J. Bovaird, L. Brill, M. Broughton, B. B. Buckley, D. A. Buell, T. Burger, B. Burkett, N. Bushnell, Y. Chen, Z. Chen, B. Chiaro, J. Cogan, R. Collins, P. Conner, W. Courtney, A. L. Crook, B. Curtin, D. M. Debroy, A. D. T. Barba, S. Demura, A. Dunsworth, D. Eppens, C. Erickson, L. Faoro, E. Farhi, R. Fatemi, L. F. Burgos, E. Forati, A. G. Fowler, B. Foxen, W. Giang, C. Gidney, D. Gilboa, M. Giustina, A. G. Dau, J. A. Gross, S. Habegger, M. C. Hamilton, M. P. Harrigan, S. D. Harrington, O. Higgott, J. Hilton, M. Hoffmann, S. Hong, T. Huang, A. Huff, W. J. Huggins, L. B. Ioffe, S. V. Isakov, J. Iveland, E. Jeffrey, Z. Jiang, C. Jones, P. Juhas, D. Kafri, K. Kechedzhi, J. Kelly, T. Khattar, M. Khezri, M. Kieferová, S. Kim, A. Kitaev, P. V. Klimov, A. R. Klots, A. N. Korotkov, F. Kostritsa, J. M. Kreikebaum, D. Landhuis, P. Laptev, K.-M. Lau, L. Laws, J. Lee, K. Lee, B. J. Lester, A. Lill, W. Liu, A. Locharla, E. Lucero, F. D. Malone, J. Marshall, O. Martin, J. R. McClean, T. Mccourt, M. McEwen, A. Megrant, B. M. Costa, X. Mi, K. C. Miao, M. Mohseni, S. Montazeri, A. Morvan, E. Mount, W. Mroczkiewicz, O. Naaman, M. Neeley, C. Neill, A. Nersisyan, H. Neven, M. Newman, J. H. Ng, A. Nguyen, M. Nguyen, M. Y. Niu, T. E. O’Brien, A. Opremcak, J. Platt, A. Petukhov, R. Potter, L. P. Pryadko, C. Quintana, P. Roushan, N. C. Rubin, N. Saei, D. Sank, K. Sankaragomathi, K. J. Satzinger, H. F. Schurkus, C. Schuster, M. J. Shearn, A. Shorter, V. Shvarts, J. Skrzynny, V. Smelyanskiy, W. C. Smith, G. Sterling, D. Strain, M. Szalay, A. Torres, G. Vidal, B. Villalonga, C. V. Heidweiller, T. White, C. Xing, Z. J. Yao, P. Yeh, J. Yoo, G. Young, A. Zalcman, Y. Zhang, and N. Zhu, Suppressing quantum errors by scaling a surface code logical qubit (2022).
- [4] C. Cohen-Tannoudji, B. Diu, and F. Laloe, Quantum mechanics, volume 1, *Quantum Mechanics* **1**, 898 (1986).
- [5] J. J. Sakurai and E. D. Commins, *Modern quantum mechanics*, revised edition (1995).
- [6] A. Blais, A. L. Grimsmo, S. M. Girvin, and A. Wallraff, Circuit quantum electrodynamics, *Reviews of Modern Physics* **93**, 025005 (2021).
- [7] P. Brooks, A. Kitaev, and J. Preskill, Protected gates for superconducting qubits, *Physical Review A* **87**, 052306 (2013).
- [8] M. Marthaler and M. Dykman, Quantum interference in the classically forbidden region: A parametric oscillator, *Phys. Rev. A* **76**, 010102 (2007).
- [9] B. Wielinga and G. J. Milburn, Quantum tunneling in a Kerr medium with parametric pumping, *Phys. Rev. A* **48**, 2494 (1993).
- [10] Y. Zhang and M. Dykman, Preparing quasienergy states on demand: A parametric oscillator, *Physical Review A* **95**, 053841 (2017).
- [11] D. Ruiz, R. Gautier, J. Guillaud, and M. Mirrahimi, Squeezed kerr quantum oscillator with multiple spectral degeneracies, *Bulletin of the American Physical Society* (2023).
- [12] S. Puri, A. Grimm, P. Campagne-Ibarcq, A. Eickbusch, K. Noh, G. Roberts, L. Jiang, M. Mirrahimi, M. H. Devoret, and S. M. Girvin, Stabilized cat in a driven nonlinear cavity: A fault-tolerant error syndrome detector, *Phys. Rev. X* **9**, 041009 (2019).
- [13] A. L. Grimsmo and S. Puri, Quantum error correction with the gottesman-kitaev-preskill code, *PRX Quantum* **2**, 020101 (2021).
- [14] N. E. Frattini, *Three-Wave Mixing in Superconducting Circuits: Stabilizing Cats with SNAILs*, Ph.D. thesis, Yale University (2021).
- [15] N. E. Frattini, R. G. Cortiñas, J. Venkatraman, X. Xiao, Q. Su, C. U. Lei, B. J. Chapman, V. R. Joshi, S. Girvin, R. J. Schoelkopf, *et al.*, The squeezed Kerr oscillator: spectral kissing and phase-flip robustness, arXiv preprint arXiv:2209.03934 (2022).
- [16] J. Venkatraman, X. Xiao, R. G. Cortiñas, A. Eickbusch, and M. H. Devoret, Static effective Hamiltonian of a rapidly driven nonlinear system, *Phys. Rev. Lett.* **129**, 100601 (2022).
- [17] A. Grimm, N. E. Frattini, S. Puri, S. O. Mundhada, S. Touzard, M. Mirrahimi, S. M. Girvin, S. Shankar, and

- M. H. Devoret, Stabilization and operation of a Kerr-cat qubit, *Nature* **584**, 205 (2020).
- [18] M. Marthaler and M. Dykman, Switching via quantum activation: A parametrically modulated oscillator, *Physical Review A* **73**, 042108 (2006).
- [19] S. Puri, S. Boutin, and A. Blais, Engineering the quantum states of light in a Kerr-nonlinear resonator by two-photon driving, *npj Quantum Information* **3**, 1 (2017).
- [20] W. Wustmann and V. Shumeiko, Parametric effects in circuit quantum electrodynamics, *Low Temperature Physics* **45**, 848 (2019).
- [21] X. Xiao, J. Venkatraman, R. G. Cortiñas, S. Chowdhury, and M. H. Devoret, in preparation (2022).
- [22] J. Venkatraman, X. Xiao, R. G. Cortiñas, and M. H. Devoret, On the static effective Lindbladian of the squeezed Kerr oscillator (2022).
- [23] M. Mirrahimi, Z. Leghtas, V. V. Albert, S. Touzard, R. J. Schoelkopf, L. Jiang, and M. H. Devoret, Dynamically protected cat-qubits: a new paradigm for universal quantum computation, *New Journal of Physics* **16**, 045014 (2014).
- [24] M. Dykman, *Fluctuating nonlinear oscillators: from nanomechanics to quantum superconducting circuits* (Oxford University Press, 2012).
- [25] F. Ong, M. Boissonneault, F. Mallet, A. Doherty, A. Blais, D. Vion, D. Esteve, and P. Bertet, Quantum heating of a nonlinear resonator probed by a superconducting qubit, *Physical Review Letters* **110**, 047001 (2013).
- [26] E. Merzbacher, The early history of quantum tunneling, *Physics Today* **55**, 44 (2002).
- [27] R. Ramos, D. Spierings, I. Racicot, and A. M. Steinberg, Measurement of the time spent by a tunnelling atom within the barrier region, *Nature* **583**, 529 (2020).
- [28] S. Fölling, S. Trotzky, P. Cheinet, M. Feld, R. Saers, A. Widera, T. Müller, and I. Bloch, Direct observation of second-order atom tunnelling, *Nature* **448**, 1029 (2007).
- [29] A. Kaufman, B. Lester, C. Reynolds, M. Wall, M. Foss-Feig, K. Hazzard, A. Rey, and C. Regal, Two-particle quantum interference in tunnel-coupled optical tweezers, *Science* **345**, 306 (2014).
- [30] A. Noguchi, Y. Shikano, K. Toyoda, and S. Urabe, Aharonov–bohm effect in the tunnelling of a quantum rotor in a linear paul trap, *Nature communications* **5**, 1 (2014).
- [31] T.-K. Hsiao, C. van Diepen, U. Mukhopadhyay, C. Reichl, W. Wegscheider, and L. Vandersypen, Efficient orthogonal control of tunnel couplings in a quantum dot array, *Phys. Rev. Applied* **13**, 054018 (2020).
- [32] M. H. Devoret, J. M. Martinis, and J. Clarke, Measurements of macroscopic quantum tunneling out of the zero-voltage state of a current-biased josephson junction, *Phys. Rev. Lett.* **55**, 1908 (1985).
- [33] R. Vijay, M. Devoret, and I. Siddiqi, Invited review article: The josephson bifurcation amplifier, *Review of Scientific Instruments* **80**, 111101 (2009).
- [34] I. Bloch, J. Dalibard, and S. Nascimbène, Quantum simulations with ultracold quantum gases, *Nature Physics* **8**, 267 (2012).
- [35] N. Goldman and J. Dalibard, Periodically driven quantum systems: effective Hamiltonians and engineered gauge fields, *Phys. Rev. X* **4**, 031027 (2014).
- [36] K. Wintersperger, C. Braun, F. N. Únal, A. Eckardt, M. D. Liberto, N. Goldman, I. Bloch, and M. Aidelsburger, Realization of an anomalous floquet topological system with ultracold atoms, *Nature Physics* **16**, 1058 (2020).
- [37] W. Wernsdorfer and R. Sessoli, Quantum phase interference and parity effects in magnetic molecular clusters, *Science* **284**, 133 (1999).
- [38] A. Alexandradinata and L. Glazman, Semiclassical theory of landau levels and magnetic breakdown in topological metals, *Phys. Rev. B* **97**, 144422 (2018).
- [39] F. Grossmann, T. Dittrich, P. Jung, and P. Hänggi, Coherent destruction of tunneling, *Phys. Rev. Lett.* **67**, 516 (1991).
- [40] H. Lignier, C. Sias, D. Ciampini, Y. Singh, A. Zenesini, O. Morsch, and E. Arimondo, Dynamical control of matter-wave tunneling in periodic potentials, *Phys. Rev. Lett.* **99**, 220403 (2007).
- [41] Y.-A. Chen, S. Nascimbène, M. Aidelsburger, M. Atala, S. Trotzky, and I. Bloch, Controlling correlated tunneling and superexchange interactions with ac-driven optical lattices, *Phys. Rev. Lett.* **107**, 210405 (2011).
- [42] S. Tomsovic and D. Ullmo, Chaos-assisted tunneling, *Physical Review E* **50**, 145 (1994).
- [43] W. K. Hensinger, H. Häffner, A. Browaeys, N. R. Heckenberg, K. Helmerson, C. McKenzie, G. J. Milburn, W. D. Phillips, S. L. Rolston, H. Rubinsztein-Dunlop, *et al.*, Dynamical tunnelling of ultracold atoms, *Nature* **412**, 52 (2001).
- [44] P. T. Cochrane, G. J. Milburn, and W. J. Munro, Macroscopically distinct quantum-superposition states as a bosonic code for amplitude damping, *Physical Review A* **59**, 2631 (1999).
- [45] D. Roberts and A. A. Clerk, Driven-dissipative quantum Kerr resonators: New exact solutions, photon blockade and quantum bistability, *Physical Review X* **10**, 021022 (2020).
- [46] T. Kanao, S. Masuda, S. Kawabata, and H. Goto, Quantum gate for a Kerr nonlinear parametric oscillator using effective excited states, *Physical Review Applied* **18**, 014019 (2022).
- [47] J.-M. Raimond and S. Haroche, *Exploring the quantum*, Oxford University Press **82**, 86 (2006).
- [48] H. Goto, Universal quantum computation with a nonlinear oscillator network, *Phys. Rev. A* **93**, 050301 (2016).
- [49] S. Puri, C. K. Andersen, A. L. Grimsmo, and A. Blais, Quantum annealing with all-to-all connected nonlinear oscillators, *Nature Communications* **8**, 15785 (2017).
- [50] F. Iachello and R. D. Levine, *Algebraic theory of molecules* (Oxford University Press, 1995).
- [51] J. Chávez-Carlos, T. L. Lezama, R. G. Cortiñas, J. Venkatraman, M. H. Devoret, V. S. Batista, F. Pérez-Bernal, and L. F. Santos, Spectral kissing and its dynamical consequences in the squeezed Kerr-nonlinear oscillator, arXiv preprint arXiv:2210.07255 (2022).
- [52] L. Gravina, F. Minganti, and V. Savona, A critical Schrödinger cat qubit (2022).
- [53] D. J. Nader, C. A. González-Rodríguez, and S. Lerma-Hernández, Avoided crossings and dynamical tunneling close to excited-state quantum phase transitions, *Phys. Rev. E* **104**, 064116 (2021).

A driven quantum superconducting circuit with multiple tunable degeneracies

Jayameenakshi Venkatraman,^{*} Rodrigo G. Cortiñas,^{*} Nicholas E. Frattini,[†] Xu Xiao, and Michel H. Devoret[‡]
Department of Applied Physics and Department of Physics, Yale University, New Haven, CT 06520, USA

(Dated: May 11, 2023)

The Supplemental text is organized as follows. In Section I, we detail the experimental calibration of Hamiltonian parameters in Eq. (2) of the main text; specifically, in Section I we present a calibration of the squeezing drive ϵ_2 and in Section II, we present a measurement of the Kerr coefficient K . In Sections III and IV, we present further experimental results supplementing Figures 2 and 4 in the main text.

In Section V and the following sections, we switch gears and detail our theoretical models. First, in Section V we formally introduce the notation employed throughout this work. We then present in Section VI two well-known squeeze-driven Kerr oscillator Hamiltonians that were introduced in the literature and comment on the relationships between them. In Section VII, we introduce the operator and phase space formulation of our particular squeeze-driven Kerr oscillator effective Hamiltonian and discuss its classical limit.

In Sections VII A, VIII and IX, we discuss distinct properties of this Hamiltonian and its eigenstates. Specifically, in Section VII A, we discuss the structure of lowest pair of well-localized wavefunctions for different Hamiltonian parameter configurations and distinguish them from those of an ordinary quadratic + quartic double-well potential. We present our semiclassical analyses, namely a WKB analysis of the tunnel splitting in Section VIII A and an overview of action quantization in Section VIII B to discuss the construction of quantized orbits. We discuss in Section IX the robustness of the degeneracies in the squeeze-driven Kerr oscillator. In Section X, we present a simple Lindblad model to capture the qualitative features of the experimentally measured transverse relaxation lifetimes T_X of the Δ variant of the Kerr-cat qubit.

Finally, in Section XI we present a self-contained tutorial and a concise introduction to the phase space formulation of quantum mechanics.

I. CALIBRATING THE SQUEEZING DRIVE AMPLITUDE ϵ_2

In this section, we present a measurement that provides an independent calibration of the squeezing drive amplitude ϵ_2 . The pulse sequence is the following: We turn on the squeezing drive at $\Delta = 0$, for a variable amount of time t during which we also turn on a Rabi drive at amplitude ϵ_x and frequency $\omega_d/2 = \omega_a$. The squeezing drive stabilizes the Schrödinger cat states with well-defined parity, and the Rabi drive induces an oscillation in this cat-qubit. We perform this experiment for different values of ϵ_2 and measure $\hat{X} = |\mathcal{C}^+\rangle\langle\mathcal{C}^-| + |\mathcal{C}^-\rangle\langle\mathcal{C}^+|$, where $|\mathcal{C}^\pm\rangle$ are the Schrödinger cat states. This protocol was introduced in [1, 2] and we refer the reader to these works for further details. The result of our experiment is shown in Figure S1A. From this experimental data, we extract a Rabi oscillation frequency Ω_x that is related to the amplitude of the Rabi drive as $\epsilon_x = \Omega_x(\epsilon_2 = 0)/2$. The photon-number at $\Delta = 0$ $|\alpha|_0^2$ is related to ϵ_x and Ω_x as $|\alpha|_0^2 = \Omega_x^2/16\epsilon_x^2$ [1, 2]. In Figure S1B, we plot the experimental data and fit for the extracted photon-number as a function of the digital control amplitude (DAC). With this result, we have a calibration of ϵ_2 as a function of the digital control amplitude (DAC) controlling the squeezing drive.

II. MEASURING THE KERR COEFFICIENT K

In this section, we detail a measurement of the Kerr coefficient K via saturation spectroscopy of the SNAIL transmon. This measurement is performed in the absence of the squeezing drive. In the following text, the letters g , e , and f index the ground, first excited, and second-excited states of the SNAIL transmon oscillator. In Figure S2, we plot the response of the readout as a function of a probe tone, whose frequency is ω_{pr} , and which we vary around the ge transition frequency of the SNAIL transmon oscillator ω_a corresponding to $\epsilon_2 = 0$. When the probe tone excites the oscillator, the readout signal due to the dispersive coupling [3] changes. The two dips in Figure S2, from left to

^{*}Electronic address: jaya.venkat@yale.edu,rodrigo.cortinas@yale.edu; these two authors contributed equally.

[†]Present address: JILA, National Institute of Standards and Technology and the University of Colorado, Boulder, Colorado, 80309, USA; Department of Physics, University of Colorado, Boulder, Colorado, 80309, USA

[‡]Electronic address: michel.devoret@yale.edu

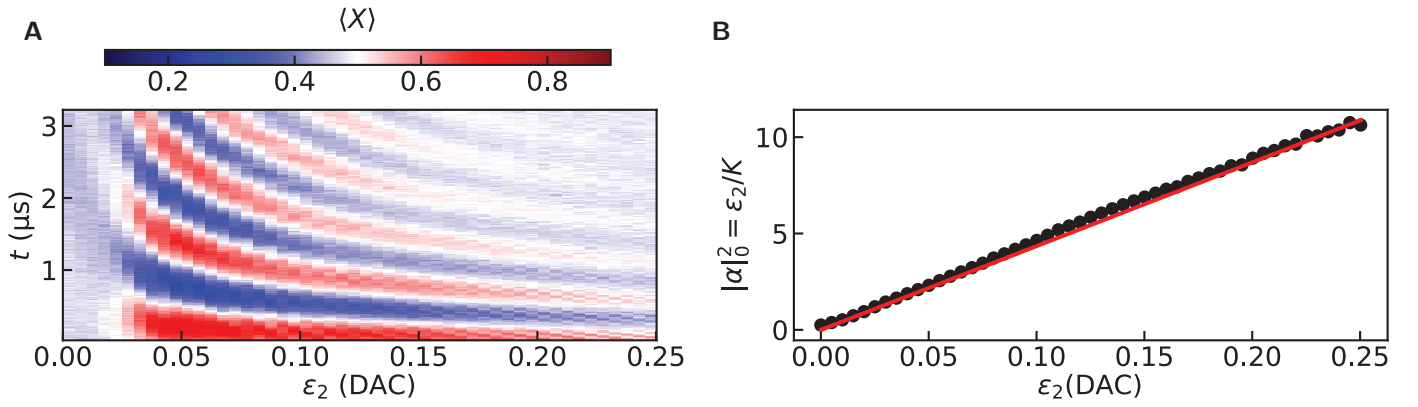


Figure S1: **Calibrating ϵ_2 with cat-Rabi oscillations.** **A** Color plot of $\langle X \rangle$ as a function of the the digital control amplitude (DAC) controlling the squeezing drive ϵ_2 and duration of the Rabi drive. We find $\epsilon_x/2\pi = 144.93$ kHz using the relation between the Rabi amplitude and Rabi frequency for $\epsilon_2 = 0$, $\epsilon_x = \Omega_x(\epsilon_2 = 0)/2$. A plot of $|\alpha|_0^2 = \epsilon_2/K = \Omega_x^2/16\epsilon_x^2$ [1, 2] as a function of ϵ_2 in DAC units. A line fit gives us a calibration of $|\alpha|_0^2 = \epsilon_2/K$ as a function of the digital control amplitude (DAC) controlling the squeezing drive.

right, correspond to a two-photon transition that excites the oscillator from g to f and to a resonant excitation of the oscillator from g to e respectively. The $gf/2$ and ge resonances are located at $(\omega_a - K)/2\pi$ and $\omega_a/2\pi$ respectively. Fitting the peaks and subtracting their locations yields a value of $K/2\pi = (329.73 \pm 4.30)$ kHz. This value is consistent with the value of $K/2\pi = 316.83$ kHz, where the latter is extracted from Figure 1E in the main text and is the value for K used throughout the article.

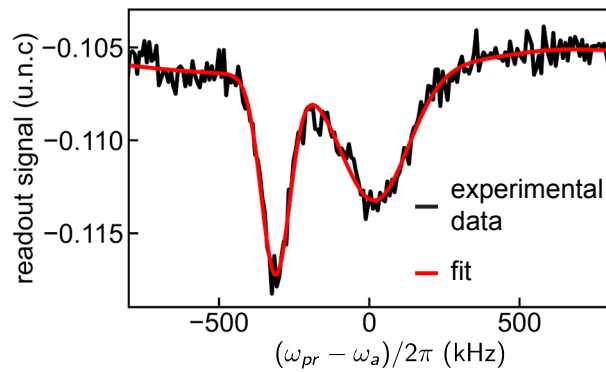


Figure S2: Readout response as a function of the frequency of the saturation (probe) tone. The two readout signal dips in black correspond, from left to right, to the $gf/2$ transition, which is expected to occur at $(\omega_a - K)/2\pi$ and to the ge transition of the SNAIL transmon, which is expected to occur at $(\omega_a)/2\pi$. Here, $gf/2$ refers to a transition induced by two photons from the probe. By fitting the experimental data, we find $K/2\pi = (329.73 \pm 4.30)$ kHz.

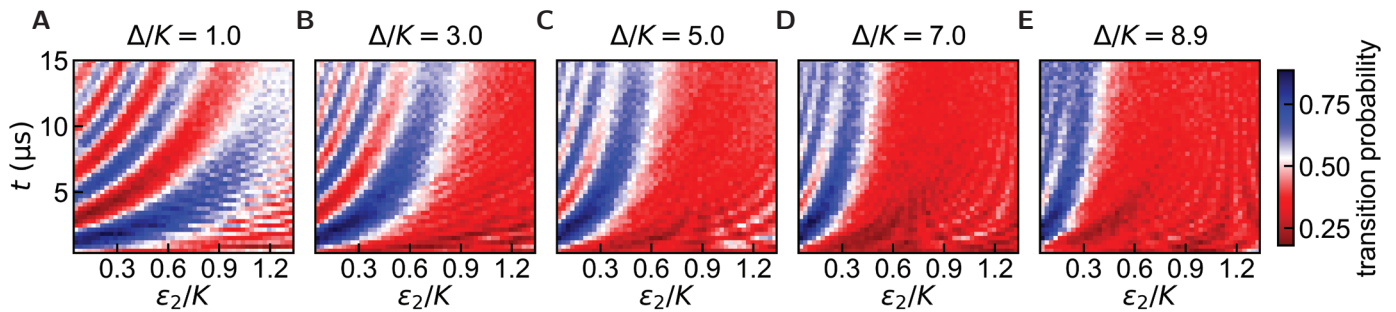


Figure S3: **Tunnel-driven Rabi oscillations in the ground state manifold and its exponential reduction as a function of ϵ_2 ; raw data.** The transition probability as a function of ϵ_2/K and time t for **A** $\Delta/K = 1$, **B** $\Delta/K = 3$, **C** $\Delta/K = 5$, **D** $\Delta/K = 7$, and **E** $\Delta/K = 9$ respectively. This corresponds to the condition of constructive interference of tunneling to occur. By progressively increasing ϵ_2 , there is a clear overall continuous reduction of the tunnel-driven Rabi oscillations.

III. EXPONENTIAL REDUCTION OF TUNNELING WITH ϵ_2

In the main text, we claim that tunneling in the ground state manifold is overall continuously reduced with ϵ_2 . The parameter ϵ_2 controls the barrier height, which is given as $(\Delta + 2\epsilon_2)^2/4K$ in the double-node phase and $2\Delta\epsilon_2/K$ in the triple-node phase. Moreover, continuing this reasoning, the larger the detuning, the faster the tunneling reduction as a function of ϵ_2 . In Figure S3, we present raw data to further support this claim. We present the measurement protocol in Figure 1C of the main text and recall it for the sake of completeness. First, we prepare, by measurement, a steady-state localized in one of the wells. Following this, we adiabatically lower the squeezing drive amplitude ϵ_2 . Lowering the value of ϵ_2 reduces the barrier depth, and thus the tunnel effect becomes observable. We then wait for a variable amount of time before adiabatically re-raising ϵ_2 to its initial value and finally do which-well readout.

In Figure S3, we present the measured transition probability as a function of ϵ_2 for **A** $\Delta/K = 1$, **B** $\Delta/K = 3$, **C** $\Delta/K = 5$, **D** $\Delta/K = 7$, and **E** $\Delta/K = 9$ respectively. It is clear from the data that the Rabi-frequency is overall continuously reduced with ϵ_2 and moreover, increasing Δ/K reduces the Rabi frequency further. We plot in Figure 2 of the main text the extracted tunneling amplitude $|\delta E|$ from our data by fitting the oscillation frequency with an exponentially decaying sinusoid. We find that the extracted tunneling amplitude is in excellent agreement with an exact diagonalization of the static effective Hamiltonian and in good agreement with a WKB prediction of the tunnel splitting within the expected regime of validity. See Figure S8 for more details.

IV. TRANSVERSE RELAXATION LIFETIME T_X MEASUREMENTS

In Figure S4, we plot the transverse relaxation lifetime T_X as a function of $\Delta^{\text{bare}} = \omega_a - \omega_d/2$ for different values of ϵ_2 . Note that the photon-number at $\Delta = 0$ is given by $|\alpha|_0^2 = \epsilon_2/K$. Importantly, for large photon-numbers $\epsilon_2/K \gtrsim 6.5$, we see that the peaks in lifetime start plateauing and even dropping. This effect is not captured by an ordinary model of the Lindblad master equation as we discuss in Section X. The degradation of the T_1 with readout power has been observed for transmon qubits [5]. But other drive-induced effects such as multiphoton nonlinear resonances are present in transmons and disentangling these various sources of lifetime degradation is nontrivial [3, 5–8]. These spurious nonlinear resonances are largely absent in this our SNAIL conducting circuit for values of $\epsilon_2/K \lesssim 5$, thanks to negligible Kerr and Stark shifts, but may plague our system for larger mean-photon numbers. Due to this reasoning, Δ might be a more effective knob to create states with large photon number [4]. Finally, the squeeze-driven Kerr oscillator provides a perfect platform to investigate lifetime degradation under drives.

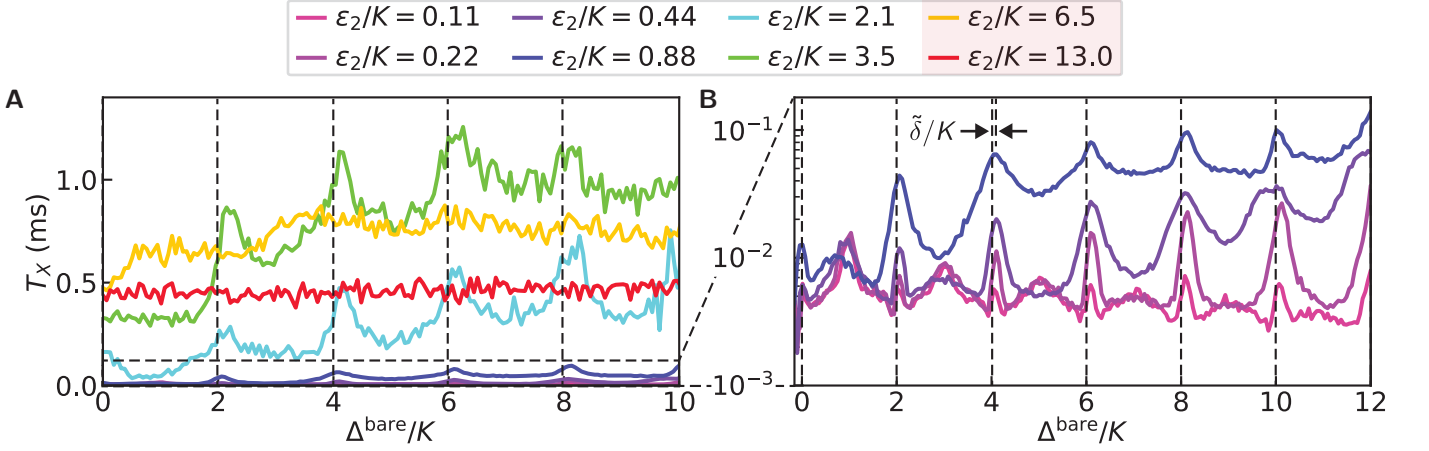


Figure S4: **Measurement of T_X as a function of $\Delta^{\text{bare}} = \omega_a - \omega_d/2$ for representative values of squeezing drive amplitude ϵ_2 .** The measurement protocol is shown in Figure 3E of the main text. We observe a degradation of T_X with increasing ϵ_2 , as indicated by red boxes in the legend, and we show representative measurements here. On the other hand, we see no degradation of T_X with increasing Δ . This measurement indicates that Δ might be a more effective knob to increase T_X than ϵ_2 for cat-states with large photon-number [4]. **B** Low-power lifetime extracted from time-resolved measurements. The data is presented as Figure 1F in the main text.

V. NOTATION

In this work, we note \hat{X} and \hat{P} the *position-like* and *momentum-like* coordinates with $[\hat{X}, \hat{P}] = i\hbar$. We build the dimensionless quadratures by introducing the zero point spread of the coordinates as X_{zps} and P_{zps} , respecting $X_{\text{zps}}P_{\text{zps}} = \hbar/2$. We further introduce the complex notation for the dimensionless quadratures as $\hat{a} = (\hat{X}/X_{\text{zps}} + i\hat{P}/P_{\text{zps}})/2$ and its conjugate operator \hat{a}^\dagger , where $[\hat{a}, \hat{a}^\dagger] = 1$ and introduce the rescaled phase space quadratures as $\hat{x} = \sqrt{\lambda/2}\hat{X}/X_{\text{zps}} = \sqrt{\lambda/2}(\hat{a} + \hat{a}^\dagger)$ and $\hat{p} = \sqrt{\lambda/2}\hat{P}/P_{\text{zps}} = -i\sqrt{\lambda/2}(\hat{a} - \hat{a}^\dagger)$, where $[\hat{x}, \hat{p}] = i\lambda$. These choices induce the definitions $x_{\text{zps}} = p_{\text{zps}} = \sqrt{\lambda/2}$. Conversely, we have $\hat{a} = (\hat{x} + i\hat{p})/\sqrt{2\lambda}$. At this point, λ is a dimensionless rescaling parameter. We will connect it with the Hamiltonian parameters later, while discussing the classical limit ($\lambda \rightarrow 0$) of our system, and thereby give it physical significance. It is also useful to compare our results with those of [9], who have performed a WKB analysis of a driven oscillator. Thus, unless otherwise specified, λ should be taken equal to unity $\lambda = 1$.

For a mechanical oscillator with mass m and spring-constant k , the small-oscillation frequency is $\omega_o = \sqrt{k/m}$ and the impedance is $Z_o = 1/\sqrt{km}$. With this, we have $X_{\text{zps}} = \sqrt{\hbar Z_o/2}$ and $P_{\text{zps}} = \sqrt{\hbar/2Z_o}$. We further remark that there is a direct correspondence between the mechanical harmonic oscillator and a linear LC circuit oscillator [3, 10, 11] under the following relations. The mechanical position coordinate \hat{X} corresponds to the circuit flux $\hat{\Phi}$, the mechanical momentum \hat{P} corresponds to the circuit charge \hat{Q} , where $[\hat{\Phi}, \hat{Q}] = i\hbar$, the mechanical oscillator frequency $\omega_o = \sqrt{k/m}$ corresponds to the circuit oscillator frequency $\omega_o = 1/\sqrt{LC}$ and the mechanical oscillator impedance $Z_o = 1/\sqrt{km}$ corresponds to the circuit oscillator impedance $Z_o = \sqrt{L/C}$ which amounts to the identification of the mechanical mass m with the circuit capacitance C and the spring constant k with the inverse inductance $1/L$. The expressions for the zero point spreads are given by $\Phi_{\text{zps}} = \sqrt{\hbar Z_o/2}$ and $Q_{\text{zps}} = \sqrt{\hbar/2Z_o}$. In circuits, it is customary to introduce [3, 12] the reduced flux and charge coordinates: $\hat{\varphi} = \sqrt{\lambda}2\pi\hat{\Phi}/\Phi_0$ and $\hat{N} = \sqrt{\lambda}\hat{Q}/2e$ so that $[\hat{\varphi}, \hat{N}] = i\lambda$, where e is the charge quantum, and $\Phi_0 = h/2e$ is the magnetic flux quantum.¹ Their respective zero point spreads $\varphi_{\text{zps}} = \sqrt{\lambda}2\pi\Phi_{\text{zps}}/\Phi_0$ and $N_{\text{zps}} = \sqrt{\lambda}Q_{\text{zps}}/2e$, and are related to the rescaled complex coordinate operators by $\hat{\varphi} = \varphi_{\text{zps}}(\hat{a}^\dagger + \hat{a})$ and $\hat{N} = -iN_{\text{zps}}(\hat{a} - \hat{a}^\dagger)$ and $\varphi_{\text{zps}}N_{\text{zps}} = \lambda/2$. We summarize this notation in the following table

¹ Note that in this case the non-dimensionalization of variables is done by fundamental constants and not by linear properties of the oscillator. This comes at the price of a slight notation asymmetry over the reduced operators the electric and mechanical oscillators.

Mechanical oscillator	Circuit oscillator
$\hat{X}; \hat{P}$	$\hat{\Phi}; \hat{Q}$
$[\hat{X}, \hat{P}] = i\hbar$	$[\hat{\Phi}, \hat{Q}] = i\hbar$
$\omega_o = \sqrt{k/m}$	$\omega_o = 1/\sqrt{LC}$
$Z_o = 1/\sqrt{km}$	$Z_o = \sqrt{L/C}$
$X_{zps} = \sqrt{\hbar Z_o/2};$ $P_{zps} = \sqrt{\hbar/2Z_o}$ $\Rightarrow X_{zps}P_{zps} = \hbar/2$	$\Phi_{zps} = \sqrt{\hbar Z_o/2};$ $Q_{zps} = \sqrt{\hbar/2Z_o}$ $\Rightarrow \Phi_{zps}Q_{zps} = \hbar/2$
$\hat{a} = \frac{1}{2} \left(\frac{\hat{X}}{X_{zps}} + i \frac{\hat{P}}{P_{zps}} \right)$	$\hat{a} = \frac{1}{2} \left(\frac{\hat{\Phi}}{\Phi_{zps}} + i \frac{\hat{Q}}{Q_{zps}} \right)$
$\hat{X} = X_{zps} (\hat{a} + \hat{a}^\dagger)$	$\hat{\Phi} = \Phi_{zps} (\hat{a} + \hat{a}^\dagger)$
$\hat{P} = -iP_{zps} (\hat{a} - \hat{a}^\dagger)$	$\hat{Q} = -iQ_{zps} (\hat{a} - \hat{a}^\dagger)$
$[\hat{a}, \hat{a}^\dagger] = 1$	$[\hat{a}, \hat{a}^\dagger] = 1$
$\hat{x} = \sqrt{\frac{\lambda}{2}} \frac{\hat{X}}{X_{zps}} = x_{zps} (\hat{a} + \hat{a}^\dagger)$	$\hat{\varphi} = \sqrt{\lambda} 2\pi \frac{\hat{\Phi}}{\Phi_0} = \varphi_{zps} (\hat{a} + \hat{a}^\dagger)$
$\hat{p} = \sqrt{\frac{\lambda}{2}} \frac{\hat{P}}{P_{zps}} = -ip_{zps} (\hat{a} - \hat{a}^\dagger)$	$\hat{N} = \sqrt{\lambda} \frac{\hat{Q}}{2e} = -iN_{zps} (\hat{a} - \hat{a}^\dagger)$
$x_{zps} = p_{zps} = \sqrt{\lambda/2}$ $\Rightarrow x_{zps}p_{zps} = \lambda/2$	$\varphi_{zps} = 2\pi\sqrt{\lambda} \frac{\Phi_{zps}}{\Phi_0}; N_{zps} = \sqrt{\lambda} \frac{Q_{zps}}{2e}$ $\Rightarrow \varphi_{zps}N_{zps} = \lambda/2$
$[\hat{x}, \hat{p}] = i\lambda$	$[\hat{\varphi}, \hat{N}] = i\lambda$
$\hat{a} = \frac{1}{2} \left(\frac{\hat{x}}{x_{zps}} + i \frac{\hat{p}}{p_{zps}} \right)$	$\hat{a} = \frac{1}{2} \left(\frac{\hat{\varphi}}{\varphi_{zps}} + i \frac{\hat{N}}{N_{zps}} \right)$
$\hat{a} = (\hat{x} + i\hat{p})/\sqrt{2\lambda}$	$\hat{a} = \left(\sqrt{\frac{\lambda}{2}} \frac{\hat{\varphi}}{\varphi_{zps}} + i\sqrt{\frac{\lambda}{2}} \frac{\hat{N}}{N_{zps}} \right) / \sqrt{2\lambda}$

VI. THE RELATIONSHIP BETWEEN DIFFERENT SQUEEZE-DRIVEN KERR OSCILLATOR MODELS IN THE LITERATURE AND THEIR CLASSICAL LIMIT

In 1993, Wielinga and Milburn [13] proposed a quantum optical model that they called *the dynamical equivalent of the double-well potential*. The interest of the problem, to them, was that their model exhibited a double-well structure in phase space, and quantum mechanical ground state tunneling between them. The Hamiltonian they addressed is

$$\hat{H}_{\text{WM}} = -K(\hat{a}^\dagger \hat{a})^2 + \epsilon_2(\hat{a}^{\dagger 2} + \hat{a}^2). \quad (\text{S1})$$

In 2017, the theoretical discovery of the Kerr-cat qubit by Puri, Boutin, and Blais [14] relied on the fact that the ground states of

$$\hat{H}_{\text{PBB}} = -K\hat{a}^{\dagger 2}\hat{a}^2 + \epsilon_2(\hat{a}^{\dagger 2} + \hat{a}^2) \quad (\text{S2})$$

are fundamentally degenerate and exhibit no tunneling between two wells found in the classical limit (see also [15]). This property can be understood by writing Eq. (S2) into the factorized form [14]

$$\hat{H}_{\text{PBB}} = -K(\hat{a}^{\dagger 2} - \epsilon_2/K)(\hat{a}^2 - \epsilon_2/K), \quad (\text{S3})$$

from which it is evident that the two coherent states $|\pm \alpha\rangle$ with $\alpha = \sqrt{\epsilon_2/K}$, which are the eigenstates of the annihilation operator \hat{a} , are also degenerate eigenstates of Eq. (S3). Since Eq. (S3) is negative-semidefinite and $\hat{H}_{\text{PBB}}|\pm \alpha\rangle = 0$, these states are the ground states.

Note that the Hamiltonians \hat{H}_{WM} and \hat{H}_{PBB} differ only by a commutator. Their shared classical limit can be written as

$$\begin{aligned} H_{\text{cl}} &= -Ka^{*2}a^2 + \epsilon_2(a^{*2} + a^2) \\ &= -K \left(\frac{x^2 + p^2}{2} \right)^2 + \epsilon_2(x^2 - p^2). \end{aligned} \quad (\text{S4})$$

Since $\hat{a}^{\dagger 2}\hat{a}^2 - (\hat{a}^\dagger \hat{a})^2 = \hat{a}^\dagger \hat{a}$, we cast the Hamiltonian

$$\hat{H} = \Delta \hat{a}^\dagger \hat{a} - K\hat{a}^{\dagger 2}\hat{a}^2 + \epsilon_2(\hat{a}^{\dagger 2} + \hat{a}^2), \quad (\text{S5})$$

where we identify that \hat{H}_{PBB} and \hat{H}_{WM} are specific instances of Eq. (S5) with $\hat{H}_{\text{PBB}} = \hat{H}|_{\Delta=0}$ and $\hat{H}_{\text{WM}} = \hat{H}|_{\Delta=-K}$. Note that taking $\Delta \neq 0$ breaks the simple factorization condition of Eq. (S3). Indeed, the presence of the $\hat{a}^\dagger \hat{a}$ term is the cause of ground state tunneling in \hat{H}_{WM} , and its absence is the cause of the complete coherent cancellation of tunneling in \hat{H}_{PBB} . The lowest eigen-manifold of Eq. (S5) is plotted in Figure S5 while the excited state manifold of Eq. (S5) is plotted in Figure S6.

In 2007, Marthaler and Dykman [9] treated a Hamiltonian similar to Eq. (S5), where Δ was kept free for a fixed ϵ_2 . This led to their prediction of periodic cancellation of tunneling amplitude for the ground state manifold as a function of Δ . Their work inspired our experiment shown in Figure 1 of the main text. We discuss in detail the mapping of their problem to ours in Section VIII.

In the following text, we discuss the quantum phase space representation of Eq. (S5).

VII. PHASE SPACE FORMULATIONS OF OUR EFFECTIVE HAMILTONIAN

Let us reconsider Eq. (S5). For its derivation starting from the circuit Hamiltonian, see appendix A of [2]. We obtain the phase space formulation of Eq. (S5) by taking the invertible Wigner transform [16] \mathfrak{W} as

$$\begin{aligned} \hat{x} &\rightarrow \mathfrak{W}\{\hat{x}\} = x; & \hat{p} &\rightarrow \mathfrak{W}\{\hat{p}\} = p; \\ \hat{a} &\rightarrow \mathfrak{W}\{\hat{a}\} = a = (x + ip)/\sqrt{2\lambda}; & \hat{a}^\dagger &\rightarrow \mathfrak{W}\{\hat{a}^\dagger\} = a^*; \\ \hat{a}^\dagger \hat{a} &\rightarrow a^* \star a = a^* a - \frac{1}{2} = \frac{x^2 + p^2}{2\lambda} - \frac{1}{2}; \\ \hat{a}^{\dagger 2} \hat{a}^2 &\rightarrow a^{*2} \star a^2 = a^{*2} a^2 - 2a^* a + \frac{1}{2} \\ &= \frac{(x^2 + p^2)^2}{4\lambda^2} - \frac{(x^2 + p^2)}{\lambda} + \frac{1}{2}; \\ \hat{a}^{\dagger 2} + \hat{a}^2 &\rightarrow a^{*2} + a^2 = \frac{(x^2 - p^2)}{\lambda}, \end{aligned} \tag{S6}$$

where the Groenewold star product [17] is given by $\mathfrak{W}\{\hat{A}\hat{B}\} = A \star B = A \exp\left(\frac{1}{2}(\overleftarrow{\partial}_a \overrightarrow{\partial}_{a^*} - \overleftarrow{\partial}_{a^*} \overrightarrow{\partial}_a)\right) B$. The Moyal bracket [16, 18] over a and a^* is defined as $\{\{A, B\}\}_{a, a^*} = A \star B - B \star A$ so that we have $\{\{a, a^*\}\} = 1$. For a pedagogical exposition on the phase space formulation of quantum mechanics, we refer the reader to Section XI and [16, 19, 20]. With Eq. (S6), we write Eq. (S5) in the phase space formulation of quantum mechanics, up-to coordinate-independent terms, as

$$H = (\Delta + 2K) \left(\frac{x^2 + p^2}{2\lambda} \right) - K \left(\frac{x^2 + p^2}{2\lambda} \right)^2 + \epsilon_2 \left(\frac{x^2 - p^2}{\lambda} \right). \tag{S7}$$

Note that Eq. (S7) is not equal to Eq. (S4) even when $\Delta = 0$ and $\lambda = 1$. We further rescale Eq. (S7) by $-K/\lambda^2$ so as to have a coefficient of order 1 for the nonlinear term and rearrange Eq. (S7) as

$$\frac{-H\lambda^2}{K} = \left(\frac{x^2 + p^2}{2} \right)^2 - \frac{2\epsilon_2\lambda}{K} \frac{x^2}{2} \left(1 + \frac{(\Delta + 2K)}{2\epsilon_2} \right) + \frac{2\epsilon_2\lambda}{K} \frac{p^2}{2} \left(1 - \frac{(\Delta + 2K)}{2\epsilon_2} \right). \tag{S8}$$

By choosing the scale of phase space $\lambda = K/2\epsilon_2$ Eq. (S8) becomes

$$\frac{-H\lambda^2}{K} = \left(\frac{x^2 + p^2}{2} \right)^2 - \frac{x^2}{2} \left(1 + \frac{\Delta}{2\epsilon_2} + 2\lambda \right) + \frac{p^2}{2} \left(1 - \frac{\Delta}{2\epsilon_2} - 2\lambda \right). \tag{S9}$$

The term proportional to λ in Eq. (S9) involves a commutator, and corresponds to the Lamb shift. The classical limit then consist in dropping this term. This is valid for $\lambda \ll \min(\Delta/2\epsilon_2, 1)$. This translates to $\Delta/K, \epsilon_2/K \gg 1$. In this limit, the WKB approximation is valid to treat Eq. (1) in the main text.

The interpretation of the Hamiltonian classical limit is that the elementary action element λ in the phase space defined by x and p must be much smaller than the typical dimensionless action of the system determined by the well-size parameters: Δ/K and ϵ_2/K . As we discuss in what follows (see section Section VII 1 and [2]), under the condition $\Delta/K, \epsilon_2/K \gg 1$, the wells of the Hamiltonian are large in the sense that they encompass many action quanta λ . Finally, note that for $\lambda \approx 1$ the classical treatment should not hold.

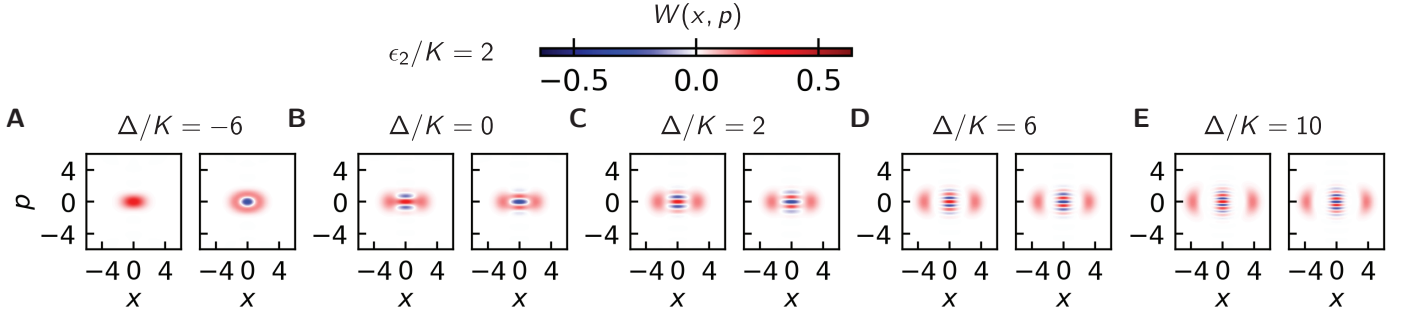


Figure S5: **Lowest eigen-manifold of the squeeze-driven Kerr oscillator** Wigner functions of lowest pair of eigenstates of Eq. (S5) (top row) for $\epsilon_2/K = 2$ and **A** $\Delta/K = -6$, **B** $\Delta/K = 0$, **C** $\Delta/K = 2$, and **D** $\Delta/K = 6$ and $\Delta/K = 10$ respectively. $\Delta/K \ll 0$, the eigenstates are squeezed. For $\Delta/K \ll 0$, increasing Δ/K yields Schrödinger cat states with increasing photon number. This phenomenon manifests as the monotonically growing baseline in transverse relaxation lifetime T_X in Figure 3 of the main text.

We call the surface for H in Eq. (S9) the metapotential of the squeeze-driven Kerr oscillator, and the classical limit for H in Eq. (S11) as the classical metapotential surface. Furthermore, as customary, we plot $-H$ rather than H to respect the familiar notion that in the presence of dissipation, stable equilibria correspond to well-bottoms rather than hill-tops.

1. Properties of the metapotential surface

In the table below, we examine the properties of the metapotential surface. For details on the number of levels inside the well, which we obtain via action quantization following the prescription of Einstein-Brillouin-Keller (EBK) [21], see Section VIII B.

Phase \rightarrow \downarrow Parameter (x, p phase space)	Double-node $-2\epsilon_2 \leq \Delta + 2K \leq 2\epsilon_2$	Triple-node $\Delta + 2K > 2\epsilon_2$
Area	$\frac{(\Delta+2K)}{K} \arccos\left(\frac{-(\Delta+2K)}{2\epsilon_2}\right) + \frac{2\epsilon_2}{K} \sqrt{1 - \left(\frac{(\Delta+2K)}{2\epsilon_2}\right)^2}$	$\frac{4\epsilon_2}{K} \sqrt{\frac{(\Delta+2K)}{2\epsilon_2} - 1} + \frac{2(\Delta+2K)}{K} \arcsin\left(\sqrt{\frac{2\epsilon_2}{(\Delta+2K)}}\right)$
Levels per well (#)	$\text{area}/2\pi - 1/2$	$\text{area}/2\pi - 1/2$
Approximation of #	$\frac{(\Delta+2K)/K}{2} + \frac{\epsilon_2/K}{\pi} - \frac{1}{2}$	$\frac{\sqrt{8\epsilon_2(\Delta+2K)}}{K\pi} - \frac{1}{2}$
Distance b/w nodes	$2\sqrt{\frac{(\Delta+2K)+2\epsilon_2}{K}}$	$2\sqrt{\frac{(\Delta+2K)+2\epsilon_2}{K}}$
Distance b/w saddles	0	$2\sqrt{\frac{(\Delta+2K)-2\epsilon_2}{K}}$
Depth of nodes	$\frac{(\Delta+2K+2\epsilon_2)^2}{4K}$	$\frac{(\Delta+2K+2\epsilon_2)^2}{4K}$
Depth of saddles	0	$\frac{(\Delta+2K-2\epsilon_2)^2}{4K}$
Depth of barrier	$\frac{(\Delta+2K+2\epsilon_2)^2}{4K}$	$\frac{2(\Delta+2K)\epsilon_2}{K}$

A. Wavefunctions of localized well states

In this section, we examine closely the wave functions of the squeeze-driven Kerr oscillator in the classically forbidden region and contrast them with those of an ordinary quadratic + quartic potential. We define the ordinary double-well Hamiltonian as

$$H = \frac{p^2}{2} + V(x), \quad \text{with} \quad V(x) = -\frac{k_2}{2}x^2 + \frac{k_4}{4}x^4,$$

where $k_2, k_4 > 0$. This potential has a saddle at $x_s = 0$, with $V(x_s) = 0$ and nodes at $x_n = \pm\sqrt{k_2/k_4}$ with the left and right well depth given by $V(x_n) = -k_2^2/(4k_4)$. The barrier height is given by $V(x_n) - V(x_s) = k_2^2/(4k_4)$.

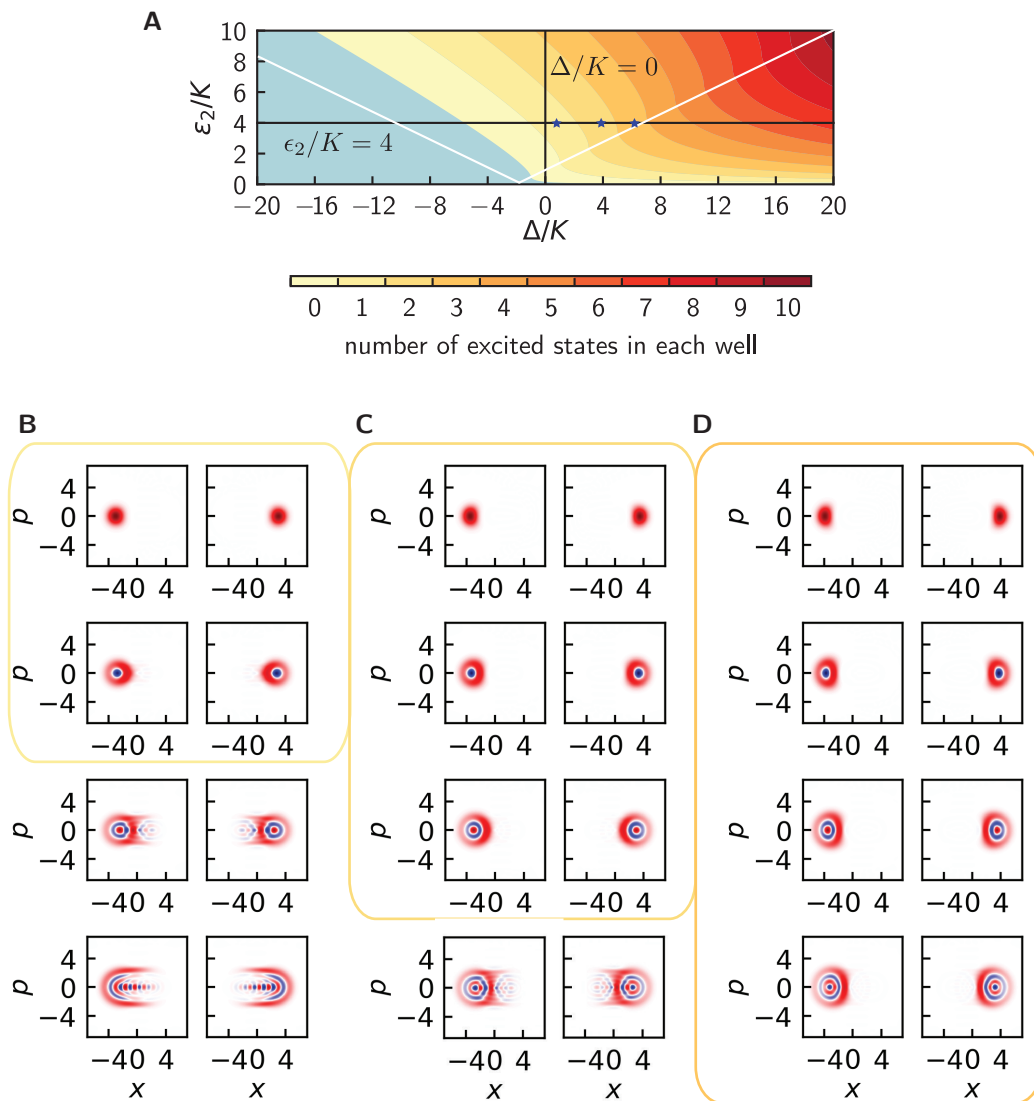


Figure S6: **Excited well states in the squeeze-driven Kerr oscillator** Localized ground and excited states in the squeeze-driven Kerr oscillator. **A** Period doubling phase diagram with equi-state contours. **B - E**. Wigner functions of exact eigenstates' superpositions, corresponding to localized states, for $\epsilon_2/K = 4$, and **B** $\Delta/K = 1$, **C** $\Delta/K = 4$, **D** $\Delta/K = 7$. The action quantization formulation, detailed in Section VIII and summarized by Eq. (S16), predicts **B** 1, **C** 2, **D** 3 excited states in each well. The Wigner functions of states outside this window are seen to have support in the other well too, and larger Δ helps localize them, thus validating the semiclassical picture discussed in Section VIII quantum mechanically.

The study of tunneling usually begins by considering a localized wave packet in one well, which is written as the superposition of the wavefunctions of the two lowest laying energy states ψ_+ and ψ_- .² Their energy difference is denoted by $\delta E = E^+ - E^-$ and the left- and right-localized wavefunctions read

$$\psi_l = \frac{\psi_+ + \psi_-}{\sqrt{2}} \quad \psi_r = \frac{\psi_+ - \psi_-}{\sqrt{2}}. \quad (\text{S10})$$

On the left column of Figure S7, we plot the left and right-localized wavefunctions in red and blue respectively for **A** $k_2 = 3$, $k_4 = 1$, **B** $k_2 = 2$, $k_4 = 1$, and **C** $k_2 = 4$, $k_4 = 2$ respectively. The wavefunctions are computed by numerical

² From a perturbation theory point of view this corresponds to the bonding and anti-bonding of the decoupled well states [22]. The zero point energy of the individual wells, in the absence of tunneling, is $E_0 = \sqrt{k_2}/2$. In the presence of tunneling the system's energies can be approximated by $E^\pm = E_0 \pm \delta E$.

diagonalization of the Hamiltonian. In the classically forbidden region, as one should expect, the wavefunctions display evanescent decay [23].

In the right column of Figure S7, we contrast the localized wavefunctions of the ordinary double-well potential with those of the squeeze-driven Kerr oscillator. The parameters Δ , K , and ϵ_2 were chosen so that a cut of the effective Hamiltonian surface at $p = 0$ yields an identical double-well potential as the left column. The wavefunctions of the full squeeze-driven Kerr oscillator are computed numerically. Importantly, **B**, **D**, and **F** show the localized wavefunctions for $\Delta/K = 0, 1$, and 2 respectively, corresponding to the destructive, constructive, and again destructive interference. Interestingly, in the classically forbidden region, in **B** and **D**, oscillations accompany decay in the wavefunction [9, 24]. This is due to the underlying driven nature of our system, providing a quartic term in momentum, which here reflects in the oscillatory nature of the wavefunctions in the classically forbidden region.

VIII. SEMICLASSICAL ANALYSIS

In [9], Marthaler and Dykman calculated the tunnel-splitting between states comprising the ground state manifold and found that the tunnel splitting vanishes periodically as a function of the drive frequency. We massage our phase-space Hamiltonian function into a form resembling Equation 5 of Marthaler and Dykman [9] by rewriting Eq. (S7) as

$$H = -\frac{K}{\lambda^2} \left[\left(\frac{x^2 + p^2}{2} \right)^2 - \frac{x^2}{2} \left(1 + \frac{\Delta}{2\epsilon_2} \right) + \frac{p^2}{2} \left(1 - \frac{\Delta}{2\epsilon_2} \right) \right] \quad (\text{S11})$$

where their parameter $\mu = (\Delta + 2K)/2\epsilon_2$.

A. WKB calculation of tunnel splitting for the ground state manifold of eq. (1)

The expression for the tunnel splitting following the analysis in [9, 24] is given as

$$\delta E = f \cos \theta \exp(-A), \quad (\text{S12})$$

where

$$\begin{aligned} f &= 2 \left(\frac{4\epsilon_2}{K} \right)^2 \left(\frac{K}{\pi(\Delta + 2K)} \right)^{1/2} \left(1 + \frac{(\Delta + 2K)}{2\epsilon_2} \right)^{5/4} \\ \theta &= \frac{\pi}{2} \left(\frac{(\Delta + 2K)}{K} - 1 \right) \\ A &= \frac{2\epsilon_2}{K} \left(\frac{(\Delta + 2K)}{2\epsilon_2} + 1 \right)^{1/2} - \frac{(\Delta + 2K)}{K} \log \left(\left(\frac{2\epsilon_2}{(\Delta + 2K)} \right)^{1/2} + \left(1 + \frac{2\epsilon_2}{(\Delta + 2K)} \right)^{1/2} \right), \end{aligned} \quad (\text{S13})$$

where, the above expression is only valid for $(\Delta + 2K)/K \gg 1$. There are two failure modes for the WKB approximation. The first condition corresponds to when $\Delta \lesssim K$, and the other is when $\epsilon_2/K \ll 1$. Note that WKB works remarkably well outside its domain of validity ($\epsilon_2/K < 1$). Compare to Figure S7, where the wavelength given by the oscillation period of the wavefunction is of the same magnitude as the potential variation set by the interwell distance. Note that we have applied the formula developed in [9] in a domain that lies beyond the parameter regime where it was produced and we find remarkable agreement with data. The comparison between measured tunneling amplitude and a WKB theory can be found in Figure S8.

B. Action quantization via Einstein-Brillouin-Keller (EBK) method

In this section, we present the semiclassical method of obtaining the number of in-well states via action quantization, following the Einstein-Brillouin-Keller method, which generalizes the notion of Bohr orbits.

First, we introduce a polar-coordinate representation of Eq. (S11), which exploits its radial symmetry, as

$$H_{\text{cl}} = \frac{\Delta r^2}{2} - \frac{K r^4}{4} + \epsilon_2 r^2 \cos 2\theta, \quad (\text{S14})$$

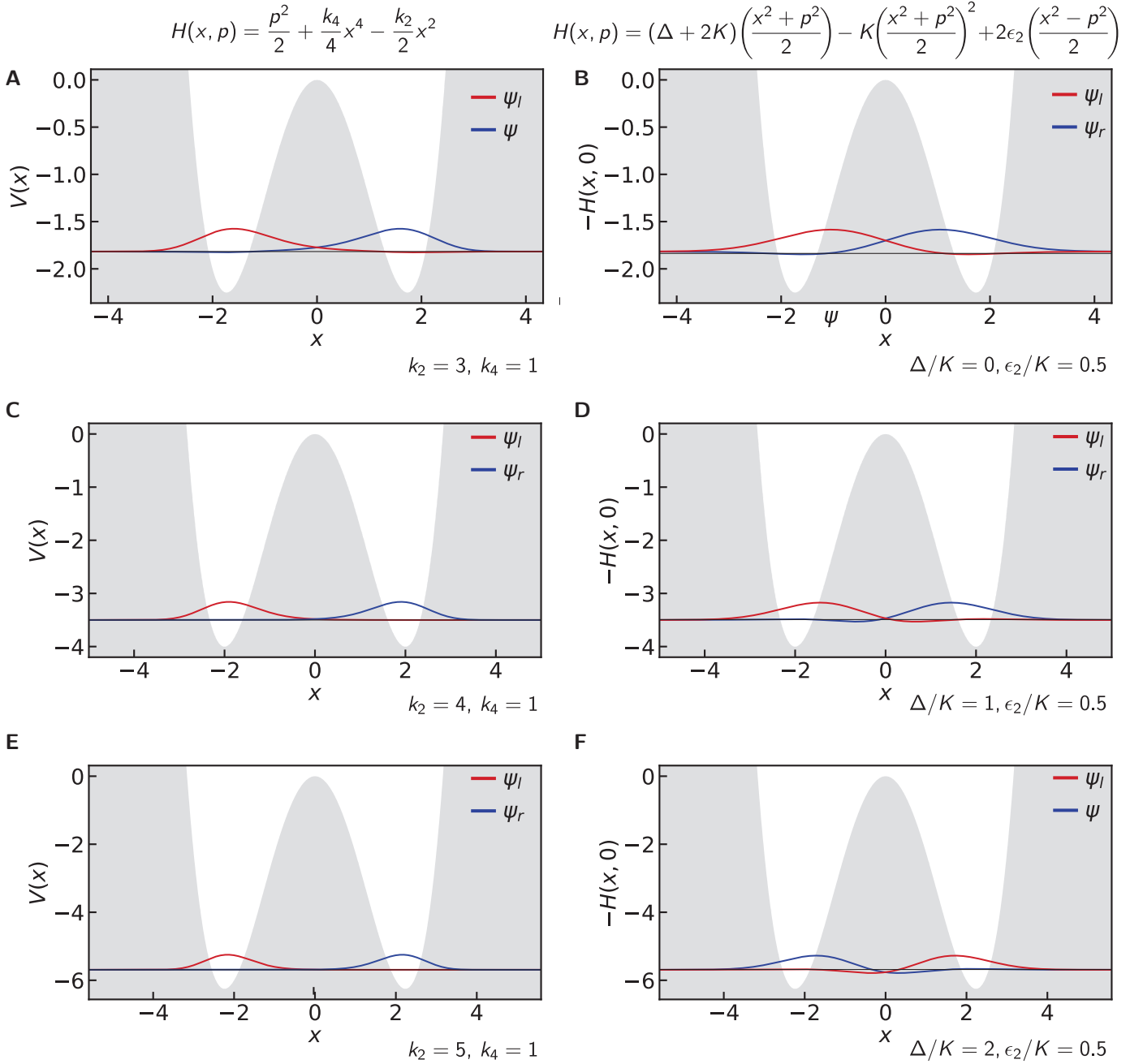


Figure S7: **Localized wavefunctions of the ground state manifold in the position basis in A, C, E an ordinary double well potential and in B, D, F for a squeeze-driven Kerr oscillator.** The Hamiltonian parameters in **A**, **C**, and **E** have been chosen to produce a double-well with the same depth and the well separation as those of **B**, **D**, and **F** respectively. The value of Δ/K is chosen to be **B** $\Delta/K = 0$, **D** $\Delta/K = 1$, and **F** $\Delta/K = 2$ corresponding to the destructive, constructive, and destructive interference of tunneling respectively. In the right panel, oscillations accompany decay of the wavefunction in the classically forbidden region, marked in grey. In the left panel, the wavefunction exhibits pure decay in the classically forbidden region. In this sense, the cancellation of tunneling amplitude in fig 1 of the main text can be understood as the destructive interference of the wavefunction in the classically forbidden region of the squeeze-driven Kerr oscillator. In [9], Marthaler and Dykman found an analytical expression for the WKB tunnel splitting of the ground state manifold. See Section VIII A for the WKB expressions for the tunnel splitting and Figure S8B and D for comparisons of the extracted tunnel splitting from experiment with their WKB theory.

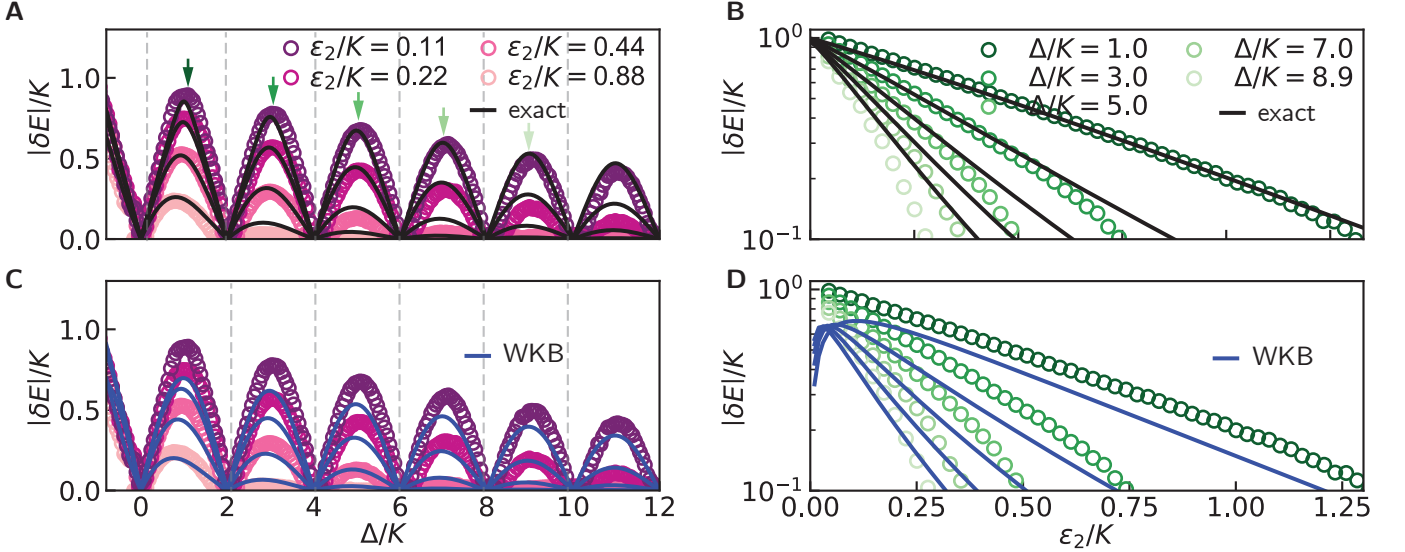


Figure S8: Experimentally extracted tunneling amplitude in the ground state manifold as a function of Δ (**A** and **C**) and ϵ_2 (**B** and **D**) compared to two different theoretical models. Dots correspond to extracted level splittings from dynamical measurements of the tunneling rate and correspond to the data presented in Figures 1C and 2 respectively. Solid lines in black in **A** and **B** are obtained via exact numerical diagonalization. Solid blue lines in **C** and **D** are obtained via a semi-classical WKB treatment developed by Marthaler and Dykman in [9, 24]. As expected, the semi-classical Hamiltonian model, in the domain of its validity $\Delta/K \gg 1$ and $\epsilon_2/K \sim 1$, agrees well with the measured data.

where $x = r \cos \theta$ and $p = r \sin \theta$, for $r \geq 0$ and $\theta \in [0, 2\pi)$.

In a semiclassical treatment, a classical orbit \mathcal{C}_j satisfying the following Einstein-Brillouin-Keller (EBK) quantization condition [21]:

$$\int_{\mathcal{C}_j} dx dp = \hbar \left(N_j + \frac{\beta_j}{4} \right), \quad (\text{S15})$$

plays a special role. On the left hand side of Eq. (S15), the action integral corresponds to the area enclosed by the contour \mathcal{C}_j . On the right hand side of Eq. (S15), the non-negative integer $N_j \geq 0$ represents a quantum number and β_j is called a Maslov index; it counts the number of caustics encountered by the contour \mathcal{C}_j . For an orbit in the Kerr-cat metapotential, we have $\beta_j = 2$. Thus the condition in Equation (S15) states that only those orbits whose enclosed area satisfy a condition given by non-negative integers n_j and $\beta_j = 2$ correspond to allowed quantum orbits.

With this condition stated, one can ask a simple question: given a set of Δ , ϵ_2 , how many in-well or bound states exist in the metapotential surface? This will be obtained by computing the number of allowed states at the separatrix, which separates bound and unbound states.

From the calculations detailed in Sections VIII B 1 and VIII B 2, we find the number of bound states as

$$N \sim \begin{cases} \frac{\Delta/K}{2} + \frac{\epsilon_2/K}{\pi} - \frac{1}{2} & -2\epsilon_2 \leq \Delta < 2\epsilon_2 \\ \frac{\sqrt{8\epsilon_2\Delta}}{K\pi} - \frac{1}{2} & \Delta \geq 2\epsilon_2. \end{cases} \quad (\text{S16})$$

We demonstrate in Fig. S6 the value of the semi-classical action quantization condition in predicting the locality in phase space of even the excited states of the squeeze-driven Kerr oscillator.

1. Separatrix area in the double-node phase: $-2\epsilon_2 \leq \Delta < 2\epsilon_2$

In the double-node phase, the separatrix has a special name called the Bernoulli's lemniscate and its equation is given as

$$r^2 = \frac{2\Delta}{K} + \frac{4\epsilon_2}{K} \cos 2\theta, \quad (\text{S17})$$

and $-\theta_c \leq \theta \leq \theta_c$, where $\theta_c = \frac{1}{2} \arccos \frac{\Delta}{2\epsilon_2}$. We compute the area of a half the lemniscate as

$$\begin{aligned}
\int_{C_j} dx p &= \frac{1}{2} \int_{-\theta_c}^{\theta_c} d\theta r^2 \\
&= \int_0^{\theta_c} d\theta \frac{2\Delta}{K} + \frac{4\epsilon_2}{K} \cos 2\theta \\
&= \frac{\Delta}{K} \arccos \left(\frac{-\Delta}{2\epsilon_2} \right) + \frac{2\epsilon_2}{K} \sqrt{1 - \left(\frac{\Delta}{2\epsilon_2} \right)^2} \\
&\sim \frac{\Delta}{K} \left(\frac{\pi}{2} + \frac{\Delta}{2\epsilon_2} \right) + \frac{2\epsilon_2}{K} \left(1 - \frac{1}{2} \left(\frac{\Delta}{2\epsilon_2} \right)^2 \right) \quad |\Delta/2\epsilon_2| \ll 1 \\
&= \frac{\pi}{2} \frac{\Delta}{K} + 2 \frac{\epsilon_2}{K}
\end{aligned} \tag{S18}$$

Note that for $\Delta = 0$, Eq. (S18) reduces to $2\epsilon_2/K$.

2. Separatrix area in the triple-node phase: $\Delta \geq 2\epsilon_2$

The separatrix in the triple-node phase is given as

$$r_{\pm}^2 = \frac{\Delta}{K} + \frac{2\epsilon_2}{K} \cos 2\theta \pm \frac{4\epsilon_2 \cos \theta}{K} \sqrt{\frac{\Delta}{2\epsilon_2} - \sin^2 \theta} \tag{S19}$$

and $-\theta_c \leq \theta \leq \theta_c$, where $\theta_c = \frac{\pi}{2}$. When plotted, this separatrix carves a bean-like shape.

Remarkably, we find an exact analytic expression for the area of this surface as

$$\begin{aligned}
\int_{C_j} dx p &= \frac{1}{2} \int_{-\theta_c}^{\theta_c} d\theta (r_+^2 - r_-^2) \\
&= \int_{-\pi/2}^{\pi/2} d\theta \frac{4\epsilon_2 \cos \theta}{K} \sqrt{\frac{\Delta}{2\epsilon_2} - \sin^2 \theta} = \frac{4\epsilon_2}{K} \int_0^1 dt \sqrt{\frac{\Delta}{2\epsilon_2} - t^2} \\
&= \frac{4\epsilon_2}{K} \sqrt{\frac{\Delta}{2\epsilon_2} - 1} + \frac{2\Delta}{K} \arcsin \left(\sqrt{\frac{2\epsilon_2}{\Delta}} \right) \\
&\sim \frac{2\sqrt{8\epsilon_2\Delta}}{K}, \quad \Delta/2\epsilon_2 \gg 1.
\end{aligned} \tag{S20}$$

IX. DEGENERACIES IN THE SQUEEZE-DRIVEN KERR OSCILLATOR

A. Robustness of degeneracies

The squeeze-driven Kerr oscillator we have engineered has the remarkable property: for $\Delta/K = 2m$, the first $m+1$ pairs of levels become decoupled from the rest of the oscillator's Hilbert space. Their eigenenergies and eigenstates become exactly solvable and present $m+1$ robust degeneracies in between states of different photon-number parity. Critically, note that the resonance condition for these degeneracies is independent of the value of the squeezing drive amplitude ϵ_2 .

First, to show this, we begin by considering the squeezing drive as a perturbation to the Kerr oscillator described by the Hamiltonian $\hat{H}_K/\hbar = \Delta \hat{a}^\dagger \hat{a} - K \hat{a}^{\dagger 2} \hat{a}^2$ which is exactly solvable: its eigenstates are Fock states $|n\rangle$ and their energies are $E_n^{(0)} = \Delta n - Kn(n-1)$, which, as a function of Δ , are lines with integer slope that we plot in the top row of Figure S9A. The even(n)-odd(l) degeneracies read $E_n = E_l$ and imply $\Delta/K = 2m$ where $m = (n+l-1)/2 \geq 0$ is any nonnegative integer. In the second row, we plot the transition spectrum with respect to the ground state at $\epsilon_2 = 0$, which, due to the choice of rotating frame, corresponds to the *highest* energy eigenstate. This is the directly experimentally observable *transition* spectrum from the *ground* state. We further note that the ground state changes with Δ ; remarkably, for $\epsilon_2 = 0$, at $\Delta/K = 2m$, the ground state is $(|m\rangle + |m+1\rangle)/\sqrt{2}$. This special property of

the squeeze-driven Kerr oscillator has technological applications [25]. In the following rows, we plot the transition spectrum for increasing values of squeezing drive amplitude ϵ_2 .

Indeed, it is clear that the squeezing drive renormalizes the energies of the Kerr oscillator. Level crossings of the Kerr oscillator with different parity remain exact crossings in the presence of the squeezing drive, since the interaction preserves parity. However, the remarkable feature is that these crossings are locked to where Δ equals an even multiple of K . In the following text, we justify this property, first via a perturbative and then provide a to-all-order proof.

1. Perturbative analysis of degeneracies

To first order in perturbation theory, we see that this even and odd Fock states remain decoupled (energy level crossings) under the parity conserving squeezing drive: $E_n^{(1)} = \langle n | (\hat{a}^{\dagger 2} + \hat{a}^2) | n+1 \rangle = 0$. The condition for crossings of consecutive levels with different parity ($E_n = E_{n+2}$) reads instead $\Delta/K = (2n+1)$. To first order in perturbation theory, the avoided crossing amplitude is $E_n^{(1)} = \epsilon_2 \sqrt{(n+1)(n+2)}$.

As a next approximation to the problem, we see the robustness of the crossings of consecutive levels with different parity (at $\Delta = 2nK$) by computing the second order correction to the n th energy levels $E_n^{(2)}$ and comparing it to the correction for the $(n+1)$ th energy level

$$E_{n+1}^{(2)} = \epsilon_2^2 \left(\frac{(n+3)(n+2)}{-2\Delta + 2K(2n+3)} + \frac{(n+1)n}{2\Delta - 2K(2n+1)} \right),$$

to find that $E_n^{(2)} = E_{n+1}^{(2)}$ for $\Delta/K = 2n$. This robustness can be seen in Figure S9A (all panels), where we see that the crossing shifts in energy but remains locked to Δ/K equal to even non-negative integers. The perturbation theory argument is easily generalized to non-consecutive level crossings and anti-crossings to this order. A similar perturbative argument was made in [25].

2. Non-perturbative analysis of degeneracies

To prove that the location of the degeneracies in Δ is independent of the squeezing drive amplitude to all orders we observe that we can write the Hamiltonian in Eq. (1) as

$$\hat{H} = \lambda_1 (\hat{a}^{\dagger 2} - \alpha^2) (\hat{a}^2 - \alpha^2) + \lambda_2 (\hat{a}^2 - \alpha^2) (\hat{a}^{\dagger 2} - \alpha^2), \quad (\text{S21})$$

where, for $\Delta/K = 2m$ (m non-negative integer), we have $\lambda_1 = -K(1+m/2)$, $\lambda_2 = mK/2$ and $\alpha = \pm \sqrt{\epsilon_2/K}$, and which is a generalization of the factorization condition proposed in [14] for $\Delta = 0$. We next consider the displaced Hamiltonian $\hat{H}^+ = \hat{D}(+\alpha)\hat{H}\hat{D}^\dagger(+\alpha)$, which brings one of the wells to the origin of phase space. In this frame, the Hamiltonian operator can be written as³

$$\begin{aligned} \hat{H}^+ = & -K (\hat{a}^{\dagger 2} \hat{a}^2 + (4\alpha^2 + 2m) \hat{a}^\dagger \hat{a}) \\ & - 2K\alpha [\hat{a}^\dagger \hat{a} - (m+1)] \hat{a}^\dagger \\ & - 2K\alpha [\hat{a}^\dagger \hat{a} - m] \hat{a}. \end{aligned}$$

While the first line is number conserving, the next two lines couple only consecutive Fock states. In matrix form, it is tridiagonal in the Fock basis $|n\rangle$. By examining the square brackets in the above expression, we see that the off-diagonal elements are exactly zero for $n = m$ and $n = m+1$. Thus, the first $m+1$ states decouple from the rest of the oscillator's Hilbert space. The finite matrix is Hermitian, negative-semidefinite, and tridiagonal so it is exactly diagonalizable. Finally, we note that in phase space, a displacement of the metapotential surface, which is mirror-symmetric about $x = 0$, is identical to an opposite displacement composed with a rotation of 180° around the origin.

³ Note that, without specializing Δ , one can directly write from Eq. (1) in the main text, or equivalently from Eq. (S21): $\hat{H}^+ = -K (\hat{a}^{\dagger 2} \hat{a}^2 + (4\alpha^2 + \Delta/K) \hat{a}^\dagger \hat{a}) - 2K\alpha [\hat{a}^\dagger \hat{a} - (\Delta/2K + 1)] \hat{a}^\dagger - 2K\alpha [\hat{a}^\dagger \hat{a} - \Delta/2K] \hat{a}$. From this expression one can directly derive the sub-space decoupling condition to be $\Delta/K = 2m$, in an exact manner, without relying in perturbative calculation or any previous knowledge existence of the resonance. The independence of the sub-space decoupling condition with respect to ϵ_2 is explicit.

Since the photon-number parity operator $\hat{\Pi} = e^{i\pi\hat{a}^\dagger\hat{a}}$ commutes with the Hamiltonian ($[\hat{\Pi}, \hat{H}] = 0$) the rotation is a symmetry of the system. Specifically; $\hat{H}^- = \hat{D}(-\alpha)\hat{H}\hat{D}^\dagger(-\alpha) \Rightarrow \hat{\Pi}\hat{H}^-\hat{\Pi} = \hat{H}^+$. We thus have two sets of equivalent⁴ $m+1$ exactly solvable eigenenergies, and $2(m+1)$ linearly independent equations⁵, which imply the existence of $m+1$ degeneracies in the spectrum for $\Delta/K = 2m$. The $2(m+1)$ eigenstates $|\psi_{k \leq m+1}^\pm\rangle = \hat{D}(\pm\alpha)|\phi_{k \leq m+1}^\pm\rangle$ of \hat{H} , where $|\phi_{k \leq m+1}^-\rangle = \hat{\Pi}|\phi_{k \leq m+1}^+\rangle$ and $\hat{H}^+|\phi_{k \leq m+1}^+\rangle = E_{k \leq m+1}|\phi_{k \leq m+1}^+\rangle$, found in this way are not orthogonal, but thanks to the two-fold degeneracy condition we can take the superposition of the right (+) and left (-) k th displaced state to get an orthogonal basis in each of the $m+1$ two-fold degenerate sub-spaces: $|\mathcal{C}_{k \leq m+1}^\pm\rangle \propto D(+\alpha)|\phi_{k \leq m+1}^+\rangle \pm D(-\alpha)|\phi_{k \leq m+1}^-\rangle$. These $2(m+1)$ pairwise-degenerate eigenstates of energy are also eigenstates of parity⁶. In this work we name these pairs of degenerate states the Δ -cats.

Note, that the robustness of the resonance condition is a peculiar symmetry property of the squeeze-driven Kerr oscillator and not a property of generic Kerr parametric oscillators. The existence of this robust degeneracies begs the question: what are the hidden symmetries associated with these degeneracies, if any? We show in Figure S9B, as an example, the spectrum of $\hat{H} = \Delta\hat{a}^\dagger\hat{a} - K\hat{a}^{\dagger 2}\hat{a}^2 + \epsilon_4(\hat{a}^{\dagger 4} + \hat{a}^4)$, where the location in Δ of the super-parity resonances depend on the value of the parametric drive amplitude ϵ_4 . Note, also, that even if the multilevel resonances in Figure S9B are displaced with the value of the parametric drive amplitude (red circles), they are locked together to a running resonance condition: the point of exact solvability is changed by the drive. The phenomenon corresponds to deep symmetries [26, 27] of these type of, as of now, engineerable bosonic Hamiltonians and will be discussed in detail in a separate publication.

X. MODELING THE MEASURED TRANSVERSE RELAXATION LIFETIME T_X

To model the transverse relaxation lifetime measurements T_X of the Kerr-cat qubit, which we also refer to as the well-switching lifetime of the Kerr-cat system, we use a standard Lindblad master equation as:

$$\partial_t \hat{\rho} = \frac{1}{i\hbar} [\hat{H}, \hat{\rho}] + \kappa(1 + \bar{n}_{\text{th}})\mathcal{D}[\hat{a}]\hat{\rho} + \kappa\bar{n}_{\text{th}}\mathcal{D}[\hat{a}^\dagger]\hat{\rho}, \quad (\text{S22})$$

where $\hat{\rho}$ describes the state of the system, $\bar{n}_{\text{th}} = 1/(\exp(\hbar\omega_a/k_B T) - 1)$ corresponds to the temperature of the environment and κ corresponds to the coupling between system and environment. The Hamiltonian \hat{H} is given by Eq. (S5) and the dissipator \mathcal{D} of the operator \hat{O} is given by $\mathcal{D}[\hat{O}]\bullet := \hat{O}\bullet\hat{O}^\dagger - (\hat{O}^\dagger\hat{O}\bullet + \bullet\hat{O}^\dagger\hat{O})/2$. In Eq. (S22), these operators correspond to single photon loss $\mathcal{D}[\hat{a}]$ and gain $\mathcal{D}[\hat{a}^\dagger]$ [28–30]. In Figure S10, we compare the data presented in Figure 3 of the main text with the lifetime extracted from Eq. (S22) for different values of n_{th} . The value of κ has been set to $\kappa = 1/T_1 = 1/20 \mu\text{s}^{-1}$. The current model seems insufficient to accurately predict the observations and more research is needed to understand the decoherence of nonlinear driven systems (see, for example, [31]). Figure S10 emphasizes the need for further measurements and a detailed modeling of possible noise sources affecting particularly driven qubits. See also the note at the end of Section XI. We also present, in Figure S11, the expected T_X as a function of ϵ_2/K for different values of Δ . This plot indicates that a Δ -Kerr-cat, in general, gives larger T_X lifetimes than a Kerr-cat ($\Delta = 0$).

⁴ Note that for the off-diagonal elements the parity transformation produces a minus sign ($\hat{\Pi}|n\rangle\langle n \pm 1|\hat{\Pi} = -|n\rangle\langle n \pm 1|$) that manifests in $\alpha \rightarrow -\alpha$: $H_{n,n\pm 1}^+ = -H_{n,n\pm 1}^-$. This leaves the finite characteristic polynomial invariant.

⁵ The elements of the finite set of eigenvectors of \hat{H}^+ , $\{|\phi_{k \leq m+1}^+\rangle\}_k$, are linearly independent from the finite set of eigenvectors of \hat{H}^- , $\{|\phi_{k \leq m+1}^-\rangle\}_k$, since they are spanned by the first $m+1$ displaced Fock states in different directions (\pm , see text). Indeed, any Fock state i that is displaced has support in all (undisplaced) Fock states j 's [?]: for $j > i$ the formula reads $|\langle j|\hat{D}(\pm 2\alpha)|i\rangle| = \left(\frac{i!}{j!}\right)^{1/2} |2\alpha|^{j-i} e^{-2|\alpha|^2} |L_i^{(j-i)}(4|\alpha|^2)| > 0$, where $L_i^{(j-i)}$ is an associated Laguerre polynomial (note that the matrix element tends to zero rapidly as $|\alpha|$, or equivalently $|\epsilon_2|$, grows, while the decoupled subspace condition, and ultimately the proof itself, is independent of these values for as long as they are non zero. If $\epsilon_2 = 0$, the proof is trivial and is given in the previous subsection). In other words, the linear independence manifests here explicitly in that $|\phi_{k \leq m+1}^\pm\rangle$ have no defined parity, yet $|\phi_{k \leq m+1}^+\rangle = \hat{\Pi}|\phi_{k \leq m+1}^-\rangle$ (note that $[\hat{\Pi}, \hat{H}^\pm] \neq 0$). Ultimately, $|\langle \phi_{k \leq m+1}^-|\hat{D}^\dagger(-\alpha)\hat{D}(+\alpha)|\phi_{k \leq m+1}^+\rangle| = |\langle \phi_{k \leq m+1}^+|\hat{D}(2\alpha)|\phi_{k \leq m+1}^+\rangle| < 1$ if $|\alpha| > 0$.

⁶ Specifically $\hat{\Pi}|\mathcal{C}_{k \leq m+1}^\pm\rangle = \pm|\mathcal{C}_{k \leq m+1}^\pm\rangle$ and are thus orthogonal. We used $\hat{D}(+\alpha)\hat{\Pi} = \hat{\Pi}\hat{D}(-\alpha)$.

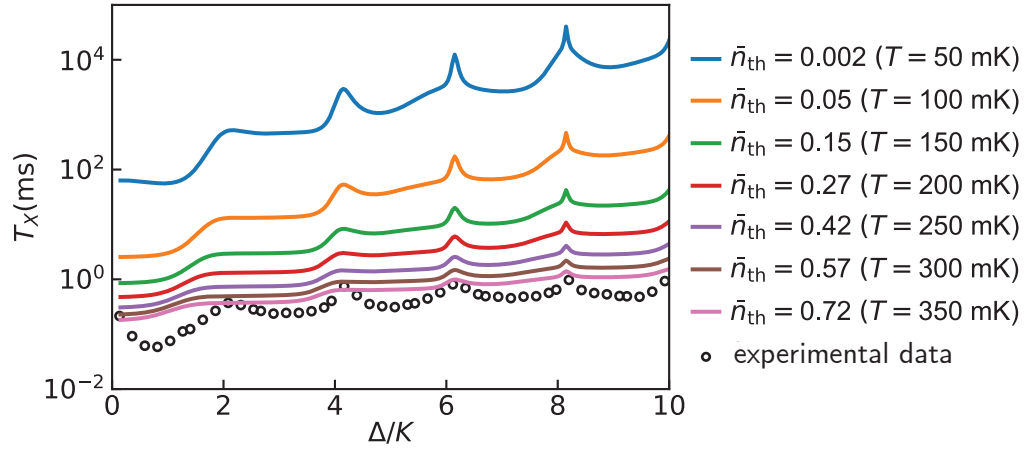


Figure S10: **Lindblad simulations of T_X as a function of Δ for different thermal populations, corresponding to Eq. (S22).** Black dots correspond to experimental data presented in Fig. 3 G in the main text. The value of κ has been taken as $\kappa = 1/T_1 = 1/20 \mu\text{s}^{-1}$ and the value of ϵ_2 has been chosen as $\epsilon_2/K = 2.17$ to match the experimental data. The solid curves take the experimentally observed ac Stark shift into account. An ordinary Lindbladian at non-zero temperature is insufficient to predict the experimental data. Beyond-RWA effects may be important to consider [31]. See also [?].

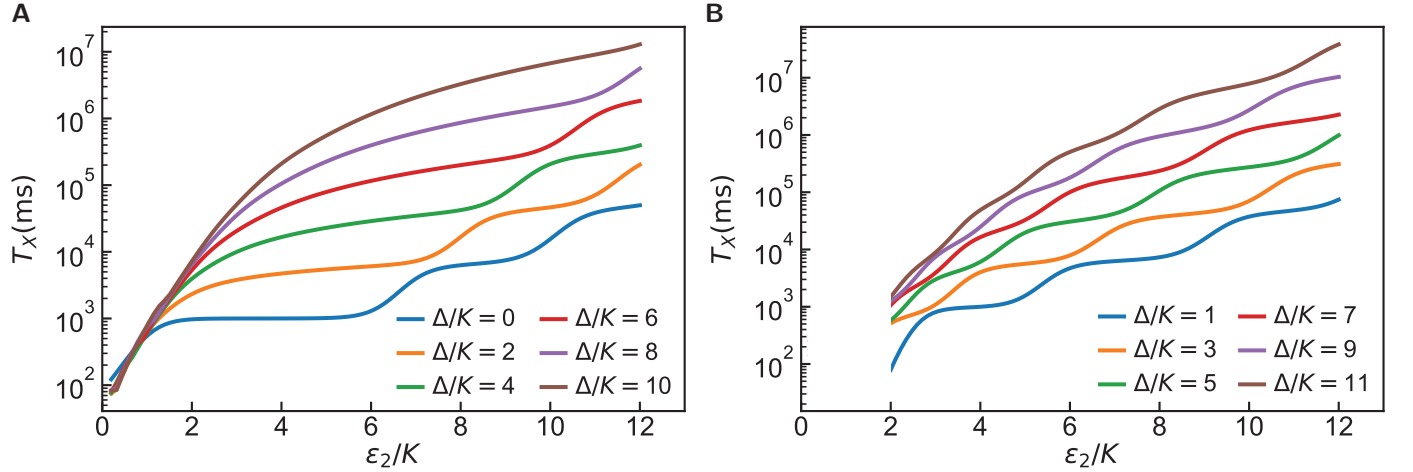


Figure S11: **Ordinary Lindblad simulations of T_X as a function of ϵ_2/K for different values of Δ/K , corresponding to Eq. (S22).** For both **A** and **B**, the value of $\kappa/K = 1/50$ and $\bar{n}_{\text{th}} = 0.05$. In **B** for $\epsilon_2/K < 2$ the lifetime is limited by ground state tunneling and is this not well captured by our simplified method.

XI. TUTORIAL ON THE PHASE SPACE FORMULATION OF QUANTUM MECHANICS

A full quantum mechanical treatment can be developed in phase space without incurring in any semiclassical approximations [16–18]. For the sake of completeness, here we provide an overview on the mapping from operator-valued Hilbert space to quantum phase space and a few elemental techniques and identities. We focus here on Wigner phase space, and showcase that the Wigner transform is more than a visualization tool for states. We note that our treatment can be equivalently extended to other phase space formulations [16, 19, 32–34].

From operator Hilbert space to Wigner phase space (and back)

The Wigner transform [35] of the density matrix $\hat{\rho}$ is the Wigner function $W(X, P)$, where X and P are standard phase space coordinates (not operators) with dimensions of position and momentum (see Section V for notation). We write this as

$$\mathfrak{W}\{\hat{\rho}\} = W(X, P).$$

Let us remind the reader of some crucial properties of the Wigner function. We have

$$\iint dX dP W(X, P) = 1, \quad (\text{S23})$$

where each integral runs from $-\infty$ to ∞ and we suppress the limits in the following text for simplicity. For a pure state, we further have

$$h \iint dX dP W(X, P)^2 = 1, \quad (\text{S24})$$

where $h = 2\pi\hbar$.

In general, we have

$$0 \leq h^{n-1} \iint dX dP W(X, P)^n \leq 1, \quad (\text{S25})$$

which corresponds to the positivity of the density matrix.

Likewise, for a generic operator \hat{F} , we introduce the phase space function $F(X, P) = \mathfrak{W}\{\hat{F}\}$.

In this framework, the average value of an Hermitian operator \hat{F} can be written as

$$\langle \hat{F} \rangle = \iint dX dP F(X, P) W(X, P). \quad (\text{S26})$$

The transformation \mathfrak{W} is invertible as appreciated by Groenewold [17]

$$\mathfrak{W}^{-1}\{W(X, P)\} = \hat{\rho}.$$

The inverse transformation \mathfrak{W}^{-1} is known as the Weyl transformation [36].

In general, the Weyl transformation is

$$\hat{\rho} = \mathfrak{W}^{-1}\{W\} = \frac{1}{h} \iiint dX dP dk dl W(X, P) e^{\frac{i}{\hbar}(k(\hat{X}-X)+l(\hat{P}-P))}, \quad (\text{S27})$$

where the characteristic function $C(l, k)$ defined as

$$C(l, k) = \iint dX dP e^{-\frac{i}{\hbar}(kX+lP)} W(X, P), \quad (\text{S28})$$

is the Fourier transform of the Wigner function and C is dimensionless.

Another useful formula is

$$W(X, P) = \frac{1}{h} \int dq e^{-iqP/\hbar} \langle X + q/2 | \hat{\rho} | X - q/2 \rangle, \quad (\text{S29})$$

where $\hat{\rho}$ is to be understood in the continuous position basis and therefore has the dimension of [1/position].

We now review simple operational rules to go from operator space to phase space functions and back without performing cumbersome integrals.

The Wigner and Weyl transformation take a particularly simple form for binomial expansions

$$\mathfrak{W}\{(\alpha\hat{X} + \beta\hat{P})^n\} = (\alpha X + \beta P)^n.$$

$$\mathfrak{W}^{-1}\{(\alpha X + \beta P)^n\} = (\alpha\hat{X} + \beta\hat{P})^n.$$

For non-symmetric expressions, the Wigner transform can be evaluated via a non-commutative Wigner phase space product, the celebrated Groenewold's star product.

A. An introduction to the star product

We introduce the star product as

$$\mathfrak{W}(\hat{F}\hat{G}) = \mathfrak{W}(\hat{F}) \star \mathfrak{W}(\hat{G}) = F(X, P) \star G(X, P), \quad (\text{S30})$$

defined as (the exponential of the Poisson bracket):

$$\begin{aligned} F \star G &= \sum_{n=0}^{\infty} \sum_{k=0}^n \frac{(-1)^k}{n!} \left(\frac{i\hbar}{2}\right)^n \binom{n}{k} \partial_P^k \partial_X^{n-k} F \times \partial_P^{n-k} \partial_X^k G \\ &\equiv F \exp\left(\frac{i\hbar}{2} \left(\overleftarrow{\partial}_X \overrightarrow{\partial}_P - \overleftarrow{\partial}_P \overrightarrow{\partial}_X\right)\right) G \\ &= FG + \frac{i\hbar}{2} \{F, G\} + \dots \end{aligned} \quad (\text{S31})$$

Here $F \overleftarrow{\partial}_X G = (\partial_X F)G$ and $F \overrightarrow{\partial}_X G = F(\partial_X G)$, and we have introduced the Poisson bracket $\{F, G\} = \partial_X F \partial_P G - \partial_P F \partial_X G$. The star product can also be conveniently expressed in terms of complex-coordinates a and a^* as

$$F \star G \equiv F \exp\left(-\frac{1}{2} \left(\overleftarrow{\partial}_{a^*} \overrightarrow{\partial}_a - \overleftarrow{\partial}_a \overrightarrow{\partial}_{a^*}\right)\right) G.$$

It generalizes to a system of many particles (or many modes) as

$$F \star G = F \exp\left(\frac{i\hbar}{2} \sum_j \left(\overleftarrow{\partial}_{X_j} \overrightarrow{\partial}_{P_j} - \overleftarrow{\partial}_{P_j} \overrightarrow{\partial}_{X_j}\right)\right) G.$$

In Fourier space the star product becomes a phase factor: $\star \rightarrow e^{i\frac{\hbar}{2}(k_X k'_P - k'_X k_P)}$ [37]. This phase corresponds to an oriented area in reciprocal phase space. This is the simplest manifestation of the noncommutativity of the algebra of quantum mechanics in phase space.

Remarkably, the scalar product associated with the star product is the usual integral in phase space. For phase space functions in the Wigner representation F and G , we have

$$\iint dXdP F(X, P) \star G(X, P) = \iint dXdP F(X, P)G(X, P). \quad (\text{S32})$$

Note however that in general for any $F(X, P)$, $G(X, P)$, and $H(X, P)$,

$$\iint dXdP F(X, P) \star G(X, P) \star H(X, P) \neq \iint dXdP F(X, P)G(X, P)H(X, P). \quad (\text{S33})$$

For non-symmetric expressions in \hat{X} and \hat{P} , the above formulae can be employed to evaluate the Wigner transform. For example

$$\mathfrak{W}\{\hat{X}\hat{P}\hat{P}\} = XP^2 + i\hbar P$$

$$\mathfrak{W}\{\hat{P}\hat{P}\hat{X}\} = XP^2 - i\hbar P$$

$$\mathfrak{W}\{\hat{P}\hat{X}\hat{P}\} = XP^2.$$

We evaluate the Weyl transform of asymmetric expressions by symmetrizing it and replacing phase space functions by their corresponding operators. For example

$$\mathfrak{W}^{-1}\{XP^2\} = \frac{1}{3}(\hat{X}\hat{P}\hat{P} + \hat{P}\hat{X}\hat{P} + \hat{P}\hat{P}\hat{X}).$$

To find the Weyl transform of a high-degree polynomial of X and P , the Weyl-symmetrized form might be too tedious and McCoy [38] provided a shortcut to obtain polynomial expressions in the phase space representation. We review McCoy's formula in the next section.

The McCoy formula for obtaining ordered operators from phase space functions

While a fully-symmetrized representation is usually inconvenient for polynomials of large degree, McCoy derived a set of formulae [38], each corresponding to a different representation of a Weyl transform. Here, we present two of them that yield operators that privilege the ordering of \hat{X} (or \hat{P}).

Consider a phase space function $F(X, P)$. Its operator-valued correspondent \hat{F} in normal order with respect to X is given by the McCoy formula [38] that reads:

$$\mathcal{F}(X, P) = e^{-i\frac{\hbar}{2}\partial_X\partial_P} F(X, P)$$

$$\mathcal{F}(X, P) = F(X, P) - \frac{i\hbar}{2}\partial_X\partial_P F(X, P) - \frac{1}{2!}\frac{\hbar^2}{2^2}\partial_X^2\partial_P^2 F(X, P) + \dots$$

$$\hat{F} = (\mathcal{N}_X \mathcal{F})|_{(\hat{X}, \hat{P})},$$

The functional (operator over real functions) \mathcal{N}_X is carried out by writing its arguments with X factors (or P factors as indicated by the subindex of \mathcal{N}) to the left in each term and replace X, P with \hat{X}, \hat{P} respectively. For example, if $F = XP$, we have $\mathcal{F} = XP - i\frac{\hbar}{2}$ which gives the correct and now ordered Hermitian expression for the operator $\hat{F} = \hat{X}\hat{P} - i\frac{\hbar}{2} = \frac{\hat{X}\hat{P} + \hat{P}\hat{X}}{2}$.

The inverse transform, is simply given $F(X, P) = e^{i\frac{\hbar}{2}\partial_X\partial_P} \mathcal{F}(X, P)$.

In terms of complex coordinates, $a = \frac{1}{\sqrt{2}}(x + ip)$ we adapt McCoy's formula [38]:

$$\mathcal{F}(a, a^*) = e^{\frac{1}{2}\partial_a\partial_{a^*}} F(a, a^*)$$

$$\hat{F} = (\mathcal{N}_{a^*} \mathcal{F})|_{(\hat{a}, \hat{a}^\dagger)}$$

to get the normal ordered (with respect to a^*) result. For example, one has classically that $\frac{1}{2}(x^2 + p^2) = a^*a$. The correct quantization reads $F = aa^* \rightarrow \mathcal{F} = aa^* + 1/2 \rightarrow \hat{F} = \hat{a}^\dagger\hat{a} + 1/2$.

Application to our Hamiltonian

If the Wigner phase space Kerr Hamiltonian reads $H = \Delta a^*a - Ka^{*2}a^2$ the corresponding operator is

$$F = a^{*2}a^2 \rightarrow \mathcal{F} = a^{*2}a^2 + 2a^*a + \frac{1}{2} \rightarrow \hat{F} = \hat{a}^{\dagger 2}\hat{a}^2 + 2\hat{a}^\dagger\hat{a} + \frac{1}{2},$$

$$\hat{H}/\hbar = (\Delta - 2K)\hat{a}^\dagger\hat{a} - K\hat{a}^{\dagger 2}\hat{a}^2,$$

where the oscillator frequency is renormalized by $2K$. This is the Lamb shift, and its origin is in the non commutativity of \hat{a} and \hat{a}^\dagger , i.e. the vacuum fluctuations.

Groenewold's theorem

Note that $\mathfrak{W}\left\{\frac{1}{i\hbar}[\hat{F}, \hat{G}]\right\} = \{\{\mathfrak{W}(\hat{F}), \mathfrak{W}(\hat{G})\}\} \neq \{\mathfrak{W}(\hat{F}), \mathfrak{W}(\hat{G})\}$. The quantum commutators do not correspond to the Poisson brackets: the theorem [17] states that such a mapping does not exist. We provide a practical consequence of the implications of this theorem to quantum Hamiltonian engineering in Appendix B of [39].

Dynamics of the Wigner function: the Moyal equation

The von-Neumann equation $\partial_t \hat{\rho} = \frac{1}{i\hbar} [\hat{H}, \hat{\rho}]$ (the density-operator version of the Schrödinger equation) transforms as

$$\partial_t W = \frac{1}{i\hbar} (H \star W - W \star H),$$

$$\partial_t W = \{\!\!\{ H, W \}\!\!\}.$$

Here $H(X, P) = \mathfrak{W}(\hat{H})$ is the Hamiltonian function and we have introduced the Moyal bracket notation [18]. We refer the reader to [20] for a derivation of the equation of motion of the Wigner function from Schrödinger's equation for the wavefunction without referring to the star product.

The exponential notation of the star product induces the name ‘‘Moyal sine bracket’’ since it can be written as

$$\partial_t W = H \frac{2}{\hbar} \sin \left(\frac{\hbar}{2} \left(\overleftarrow{\partial}_X \overrightarrow{\partial}_P - \overleftarrow{\partial}_P \overrightarrow{\partial}_X \right) \right) W.$$

Note that the Moyal equation is identical to Liouville equation plus quantum corrections coming from the expansion of the sine to higher orders of \hbar .

$$\partial_t W = \{H, W\} + \mathcal{O}(\hbar^2).$$

Interestingly, there is no corrections to $\mathcal{O}(\hbar)$. Importantly, the quantum corrections are proportional to \hbar^2 and to the nonlinear terms in the Hamiltonian. For quadratic Hamiltonians, all the quantum corrections vanish: the higher-order derivatives exterminate low-order polynomials (see the Appendix of [2]). Specifically, Gaussian transformations, i.e., those generated by quadratic Hamiltonians in the phase space coordinates, are classical in the sense that they are ruled by only the Poisson bracket. Thus, they would not develop negativities in the Wigner distribution if none would be present at the beginning.

Phase space formulation for open quantum systems

So far, we have only discussed the phase space formulation for closed quantum systems. Indeed, one can extend the treatment to open systems as we demonstrate below. The Lindblad equation for single photon loss is given by

$$\partial_t \hat{\rho} = \frac{1}{i\hbar} [\hat{H}, \hat{\rho}] + \kappa \hat{a} \hat{\rho} \hat{a}^\dagger - \frac{\kappa}{2} (\hat{a}^\dagger \hat{a} \hat{\rho} + \hat{\rho} \hat{a}^\dagger \hat{a}). \quad (\text{S34})$$

Using Eq. (S30) and Eq. (S31), we get the phase space formulation of Eq. (S34) as

$$\mathfrak{W}\{\partial_t \hat{\rho}\} = \partial_t W,$$

$$\begin{aligned} \mathfrak{W}\left\{\frac{1}{i\hbar} [\hat{H}, \hat{\rho}]\right\} &= \{\!\!\{ \mathfrak{W}(\hat{H}), \mathfrak{W}(\hat{\rho}) \}\!\!\} \\ &= \{\!\!\{ H, W \}\!\!\} \end{aligned}$$

$$\begin{aligned} \mathfrak{W}\{\hat{a} \hat{\rho} \hat{a}^\dagger\} &= a \star W \star a^* \\ &= a W a^* + \frac{1}{2} \partial_a W + \frac{1}{2} (\partial_{a^*} (W a^*) + \frac{1}{2} \partial_{aa^*}^2 W) \end{aligned}$$

$$\begin{aligned} \mathfrak{W}\{\hat{a}^\dagger \hat{\rho}\} &= \left(a^* a - \frac{1}{2} \right) \star W \\ &= a W a^* - \frac{1}{2} W + \frac{1}{2} (a^* \partial_{a^*} W - a \partial_a W) - \frac{1}{4} \partial_{aa^*}^2 W \end{aligned}$$

$$\begin{aligned}\mathfrak{M}\{\hat{\rho}\hat{a}^\dagger\hat{a}\} &= W \star \left(a^* a - \frac{1}{2} \right) \\ &= aW a^* - \frac{1}{2}W - \frac{1}{2}(a^* \partial_{a^*} W - a \partial_a W) - \frac{1}{4} \partial_{aa^*}^2 W\end{aligned}$$

Gathering all terms one directly gets

$$\partial_t W = \{H, W\} + \frac{\kappa}{2} (\partial_{aa^*}^2 + \partial_a a + \partial_{a^*} a^*) W.$$

It is convenient to translate the above to x, p space

$$\partial_t W = \{H, W\} + \frac{\kappa}{2} (\partial_x^2 + \partial_p^2 + \partial_x x + \partial_p p) W. \quad (\text{S35})$$

By expressing the equation in x, p space in Eq. (S35), the diffusion terms $\propto (\partial_x^2 + \partial_p^2)$ and the drag terms $\propto (\partial_x x + \partial_p p)$ associated to the fluctuation and the dissipation become evident. Note, that the Moyal sine bracket has only odd derivatives: the diffusion $(\partial_x^2 + \partial_p^2)$ cannot be canceled by Hamiltonian dynamics.

For finite temperature \bar{n}_{th} , the Lindblad master equation is

$$\partial_t \hat{\rho} = \frac{1}{i\hbar} [\hat{H}, \hat{\rho}] + \kappa(1 + \bar{n}_{\text{th}}) \mathcal{D}[\hat{a}] \hat{\rho} + \kappa \bar{n}_{\text{th}} \mathcal{D}[\hat{a}^\dagger] \hat{\rho}, \quad (\text{S36})$$

where the dissipator \mathcal{D} of the operator \hat{O} is given by $\mathcal{D}[\hat{O}] \bullet := \hat{O} \bullet \hat{O}^\dagger - (\hat{O}^\dagger \hat{O} \bullet + \bullet \hat{O}^\dagger \hat{O})/2$.

It is straightforward to show that in the phase space formulation, Eq. (S36) reads

$$\partial_t W = \{H, W\} + \frac{\kappa}{2} (\partial_a a + \partial_{a^*} a^*) W + \kappa \left(\frac{1}{2} + \bar{n}_{\text{th}} \right) \partial_{a^* a}^2 W, \quad (\text{S37})$$

which reads in x, p space as

$$\partial_t W = \{H, W\} + \frac{\kappa}{2} (\partial_x x + \partial_p p) W + \frac{\kappa}{2} \left(\frac{1}{2} + \bar{n}_{\text{th}} \right) (\partial_x^2 + \partial_p^2) W. \quad (\text{S38})$$

Equation (S38) is the quantum version of the Fokker-Planck equation, with the Poisson bracket replaced by the Moyal bracket and a quantum diffusion term corresponding to the zero point spread.

Note that for the Hamiltonian corresponding to Eq. (S5), the solution for W from Eq. (S38) will not yield the Boltzmann distribution in steady state, which perhaps is not surprising for an out-of-equilibrium driven problem [40].

-
- [1] A. Grimm, N. E. Frattini, S. Puri, S. O. Mundhada, S. Touzard, M. Mirrahimi, S. M. Girvin, S. Shankar, and M. H. Devoret, *Nature* **584**, 205 (2020).
- [2] N. E. Frattini, R. G. Cortiñas, J. Venkatraman, X. Xiao, Q. Su, C. U. Lei, B. J. Chapman, V. R. Joshi, S. Girvin, R. J. Schoelkopf, et al., arXiv preprint arXiv:2209.03934 (2022).
- [3] A. Blais, A. L. Grimsmo, S. M. Girvin, and A. Wallraff, *Reviews of Modern Physics* **93**, 025005 (2021).
- [4] D. Roberts and A. A. Clerk, *Physical Review X* **10**, 021022 (2020).
- [5] D. Sank, Z. Chen, M. Khezri, J. Kelly, R. Barends, B. Campbell, Y. Chen, B. Chiaro, A. Dunsworth, A. Fowler, et al., *Physical review letters* **117**, 190503 (2016).
- [6] R. Shillito, A. Petrescu, J. Cohen, J. Beall, M. Hauru, M. Ganahl, A. G. M. Lewis, G. Vidal, and A. Blais, *Dynamics of transmon ionization* (2022).
- [7] J. Cohen, A. Petrescu, R. Shillito, and A. Blais, *Reminiscence of classical chaos in driven transmons* (2022).
- [8] A. Petrescu, M. Malekakhlagh, and H. E. Türeci, *Physical Review B* **101**, 134510 (2020).
- [9] M. Marthaler and M. Dykman, *Physical Review A* **76**, 010102 (2007).
- [10] M. H. Devoret et al., *Les Houches, Session LXIII* **7**, 133 (1995).
- [11] S. M. Girvin, *Quantum machines: measurement and control of engineered quantum systems* pp. 113–256 (2014).
- [12] M. H. Devoret, *Journal of Superconductivity and Novel Magnetism* **34**, 1633 (2021).
- [13] B. Wielinga and G. J. Milburn, *Phys. Rev. A* **48**, 2494 (1993), URL <https://link.aps.org/doi/10.1103/PhysRevA.48.2494>.
- [14] S. Puri, S. Boutin, and A. Blais, *npj Quantum Information* **3**, 1 (2017).
- [15] P. T. Cochrane, G. J. Milburn, and W. J. Munro, *Physical Review A* **59**, 2631 (1999).
- [16] T. L. Curtright, D. B. Fairlie, and C. K. Zachos, *A concise treatise on quantum mechanics in phase space* (World Scientific Publishing Company, 2013).

- [17] H. J. Groenewold, in On the principles of elementary quantum mechanics (Springer, 1946), pp. 1–56.
- [18] J. E. Moyal, in Mathematical Proceedings of the Cambridge Philosophical Society (Cambridge University Press, 1949), vol. 45, pp. 99–124.
- [19] M. Hillery, R. F. O’Connell, M. O. Scully, and E. P. Wigner, *Physics reports* **106**, 121 (1984).
- [20] W. B. Case, *American Journal of Physics* **76**, 937 (2008).
- [21] M. C. Gutzwiller, Chaos in classical and quantum mechanics, vol. 1 (Springer Science & Business Media, 2013).
- [22] L. D. Landau and E. Lifshitz, Course of theoretical physics, quantum mechanics non-relativistic theory (Pergamon, 1991).
- [23] D. J. Griffiths and D. F. Schroeter, Introduction to quantum mechanics (Cambridge university press, 2018).
- [24] M. Marthaler and M. Dykman, *Physical Review A* **73**, 042108 (2006).
- [25] Y. Zhang and M. I. Dykman, *Phys. Rev. A* **95**, 053841 (2017).
- [26] F. Iachello, in Neutron Capture Gamma-Ray Spectroscopy (Springer, 1979), pp. 23–35.
- [27] F. Iachello, in Lie Algebras and Applications (Springer, 2015), pp. 53–56.
- [28] H. J. Carmichael, Statistical methods in quantum optics 1: master equations and Fokker-Planck equations, vol. 1 (Springer Science & Business Media, 1999).
- [29] H. J. Carmichael, Statistical methods in quantum optics 2: Non-classical fields (Springer Science & Business Media, 2009).
- [30] H.-P. Breuer, F. Petruccione, et al., The theory of open quantum systems (Oxford University Press on Demand, 2002).
- [31] J. Venkatraman, X. Xiao, R. G. Cortiñas, and M. H. Devoret, arXiv preprint arXiv:2209.11193 (2022).
- [32] J.-M. Raimond and S. Haroche, *Oxford University Press* **82**, 86 (2006).
- [33] R. R. Puri et al., Mathematical methods of quantum optics, vol. 79 (Springer, 2001).
- [34] X. Xiao, J. Venkatraman, R. G. Cortiñas, S. Chowdhury, and M. H. Devoret, in preparation (2022).
- [35] E. Wigner, *Phys. Rev.* **40**, 749 (1932).
- [36] H. Weyl, The Theory of Groups and Quantum Mechanics (E. P. Dutton & Co., 1931).
- [37] C. Zachos, *Journal of Mathematical Physics* **41**, 5129 (2000).
- [38] N. H. McCoy, *Proceedings of the National Academy of Sciences* **18**, 674 (1932).
- [39] J. Venkatraman, X. Xiao, R. G. Cortiñas, A. Eickbusch, and M. H. Devoret, *Physical Review Letters* **129**, 100601 (2022).
- [40] M. Dykman, Fluctuating nonlinear oscillators: from nanomechanics to quantum superconducting circuits (Oxford University Press, 2012).